MOLECULAR BIOLOGY

Dose-dependent hormone actions at estrogen receptor enhancers specify distinct molecular and biological outcomes

Hyung Bum Kim[1,2], Tulip Nandu[1], Yoon Jung Kim[3], Cristel V. Camacho[1,4], W. Lee Kraus[1,2,4]*

Adult women are typically exposed to 17β-estradiol (E2) concentrations of ~100 to 200 pM, yet most cell-based studies use 100 nM. We determined the molecular effects of E2 concentrations spanning six orders of magnitude (1 pM to 100 nM) in breast cancer cells. Estrogen receptor α (ERα) enhancers formed at low physiological doses of E2 (1 to 100 pM) are mechanistically distinct from those that form at high pharmacological doses (10 to 100 nM). They (i) form in open chromatin bound by FOXA1, (ii) are clustered within topologically associated domains, (iii) produce enhancer RNAs enriched with functional enhancer RNA regulatory motifs, and (iv) drive expression of proliferation genes with promoter-proximal paused RNA polymerase II and distinct co-regulator enrichment. Low-dose ERα enhancer usage is elevated in patients who have breast cancer with poor responses to aromatase inhibitors, likely as a continued response to low circulating levels of E2. Collectively, our results identify mechanistic differences between low- and high-dose ERα enhancers that specify distinct biological outcomes.

INTRODUCTION

Estrogens are a class of steroid hormones required for the normal development and function of reproductive organs, mammary glands, bone, heart, vasculature, adipose, and key cell types in the central nervous system (*1*–*5*). Estrogens also play key roles in diseases associated with the same tissues and contribute to a host of pathologies with unique onset, frequency, and presentation in women, such as cardiovascular, neuronal, and immune disease, as well as aging and cancer (*3*–*7*). Within an individual, estrogen levels may fluctuate markedly and acutely across multiple timescales—hours, days, months, years, and decades—and can be influenced by physiology, pathology, and therapy [(*8*–*10*) and references therein]. The circulating blood levels of 17β-estradiol (E2), the most potent naturally occurring estrogen, fluctuate depending on life stage, from nonpregnant lows of ~70 pM to highs of ~1.8 nM, rarely exceeding these levels (prepubertal, ~70 pM; menstrual, ~220 pM to 1.8 nM; pregnant, 8 to 50 nM; postmenopausal, ~0 to 110 pM) (Fig. 1A) (*11*, *12*). Despite this understanding, a higher-resolution characterization of the genomic and molecular mechanisms that underlie the cellular response to physiological doses of E2 is needed.

Many of the biological actions of estrogens are mediated by estrogen receptor α (ERα), a nuclear receptor, which functions primarily as a ligand-regulated, DNA-binding transcription factor (TF) in the nuclei of estrogen-responsive cells (*13*–*15*). Studies of nuclear receptors have played a key role in our understanding of enhancers, including key concepts such as nuclease [e.g., deoxyribonuclease I (DNase I)] hypersensitivity (*16*–*20*), co-regulators (*21*–*25*), distal enhancers, and chromatin looping (*26*, *27*). Estrogens act as potent mitogens in ERα-positive breast cancers (ER+ BC), eliciting a rapid and robust genomic response through ERα. Expression of nearly half of the genome is regulated by E2 stimulation in ER+ MCF-7 breast cancer cells (*28*, *29*), making them a powerful system to study the genomic actions of hormonal signaling.

ERα is a TF that resides in the nuclei of cells even in the absence of estrogen. It dimerizes after binding its ligands, including the predominant naturally occurring estrogen E2, and binds to many thousands of ERα binding sites (ERBSs) across the genome, collectively called the ERα "cistrome" (*15*, *30*–*33*). ERBSs may be prebound by "pioneer" TFs [e.g., forkhead box A1 (FOXA1)] before estrogen treatment, which facilitate the binding of ERα to chromatin (*34*, *35*). Many ERBSs contain a DNA sequence motif called the estrogen response element (ERE) (*14*). The binding of ERα to genomic DNA promotes the coordinated recruitment of co-regulator proteins [e.g., nuclear receptor coactivators (NCOAs)] that establish active enhancers, leading to chromatin looping and target gene transcription (*29*, *36*–*39*). Enrichment of molecular features, including certain histone modifications [e.g., H3 lysine 27 acetyl (H3K27ac)], coactivators [e.g., p300/CREB (cAMP response element–binding protein) binding protein (CBP) and Mediator], RNA polymerase II (Pol II), an open chromatin architecture (e.g., DNase I hypersensitivity), and looping to target gene promoters, marks or identifies active enhancers (*29*, *40*–*42*). The transcriptional effects of estrogen are rapid, on the order of minutes, resulting in transcription at both target genes and their enhancers (*28*, *29*, *43*, *44*). ERBSs are also spatially organized within large clusters that work in concert to control gene regulatory networks (*45*, *46*). Furthermore, these ERα enhancer clusters are organized within topologically associated domains (TADs) that form spatially constrained regulatory regions (*37*, *47*–*49*).

Although the importance of dose and the frequency and duration of administration have long been recognized as important aspects of the therapeutic use of steroid hormones (*50*–*52*), the effects of lower physiological doses of E2 and acute treatment on the molecular and genomic end points listed above are not well characterized. Previous genomic studies of nuclear receptor function have relied primarily on E2 treatments ≥5 nM E2, with few examining

[1]The Laboratory of Signaling and Gene Expression, Cecil H. and Ida Green Center for Reproductive Biology Sciences, University of Texas Southwestern Medical Center, Dallas, TX 75390, USA. [2]Program in Genetics, Development and Disease, Graduate School of Biomedical Sciences, University of Texas Southwestern Medical Center, Dallas, TX 75390, USA. [3]Children's Medical Center Research Institute, University of Texas Southwestern Medical Center, Dallas, TX 75390, USA. [4]The Section of Laboratory Research, Department of Obstetrics and Gynecology, University of Texas Southwestern Medical Center, Dallas, TX 75390, USA.
*Corresponding author. Email: lee.kraus@utsouthwestern.edu

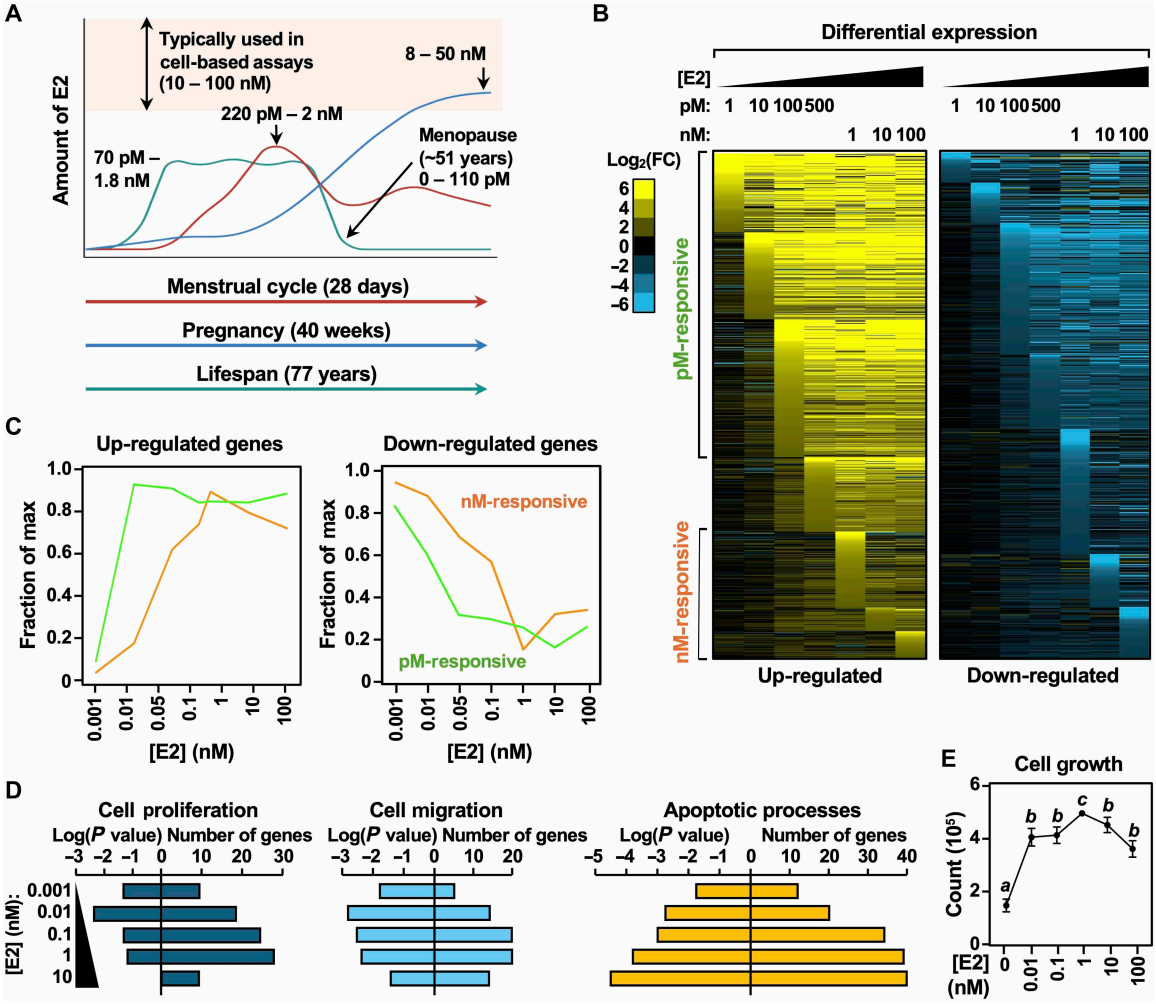

Fig. 1. Dose-dependent effects of E2 on ERα-mediated gene expression. (**A**) Schematic diagram showing the ranges of physiological E2 concentrations in women during the mensural cycle, pregnancy, and lifetime. The highlighted region shows the concentrations typically used in biochemical assays. (**B**) Heatmap representations of gene expression as determined by RNA-seq after treatment with increasing concentrations of E2 (1 pM to 100 nM) for 2 hours showing up-regulated genes (left) and down-regulated genes (right). Genes are clustered by the dose at which the first significant response occurred ($P < 0.01$) in descending order of fold change within the cluster. Gene groups are labeled in aggregate as picomolar-responsive (1 to 100 pM E2) and nanomolar-responsive (1 to 100 nM E2). FC, fold change. (**C**) Line graphs showing the relative expression of genes (fraction of maximum) within each dosage group for up-regulated (left) and down-regulated (right) over a range of E2 concentrations. (**D**) GO analyses showing the number of genes and *P* values for the terms cell proliferation, cell migration, and apoptotic process over a range of E2 concentrations. (**E**) Line graph showing cell growth at day 5 of E2 treatment as determined by live cell counts over a range of E2 concentrations. Each point represents the mean ± SEM; $n = 3$; Points marked with different letters are significantly different from each other. One-way ANOVA, $P < 0.05$.

doses in the picomolar range (table S1) (*53*). Here, we describe studies examining the dose effects of E2 for concentrations spanning six orders of magnitude (1 pM to 100 nM) in MCF-7 cells. We found that ERα enhancers formed at low (picomolar) physiological doses are mechanistically and functionally distinct from those that form at high (nanomolar) pharmacological doses.

RESULTS

Different E2 dose sensitivities for the expression of distinct sets of estrogen target genes

To determine how ERα-expressing cells respond to different doses of E2, we treated MCF-7 human breast cancer cells with a range of physiological to pharmacological doses of E2 over six orders of magnitude (1 pM to 100 nM) and examined the changes in gene expression by RNA sequencing (RNA-seq). We observed up-regulation or down-regulation of distinct sets of genes even at the lowest doses of E2 (Fig. 1B). At each successive dose, additional regulated genes were added to the previous gene sets (Fig. 1B). This analysis defined distinct sets of genes responsive to lower, physiological concentrations of E2 ("picomolar-responsive genes") or higher, pharmacological concentrations of E2 ("nanomolar-responsive genes") (fig. S1, A and B), with a clear dose shift evident for the different gene sets when expressed in aggregate (Fig. 1C; see table S2 for a glossary of E2 dose terms used herein).

Pathway analysis using the Kyoto Encyclopedia of Genes and Genomes (KEGG) showed enrichment of a number of terms related to cancer pathology in the picomolar-responsive gene group, including

DNA replication, Wnt signaling, basal-cell carcinoma, and proteoglycans in cancer (fig. S1C). In contrast, a thematically broader range of terms, including cellular senescence, insulin signaling, mitogen-activated protein kinase signaling, and tight junctions, was enriched in the nanomolar-responsive group (fig. S1D). Gene ontology (GO) analyses showed dose-dependent enrichment of cancer-related terms, with cell proliferation and cell migration showing greater enrichment with increasing concentrations of E2, except at the highest dose (100 nM) (Fig. 1D). Cell growth assays across a range of E2 concentrations showed a corresponding trend, with the highest dose (100 nM) eliciting a submaximal response compared to 1 nM E2 (Fig. 1E). Together, these analyses reveal key features of the E2 dose response: (i) E2 is a potent regulator of ERα-dependent gene expression and cell growth, with robust responses occurring at picomolar concentrations of E2, and (ii) E2 responses saturate at nanomolar concentrations of E2, with the highest doses not necessarily eliciting the greatest responses.

To determine whether a prolonged treatment with a low dose of E2 would eventually achieve the level of response from a high dose of E2, we treated MCF-7 cells with 10 pM or 10 nM E2 over a 6-hour time course and measured the expression for a selected set of low and high dose–sensitive genes by reverse transcription quantitative polymerase chain reaction (RT-qPCR). We observed no changes in the dose-sensitivity profiles of the genes at longer treatment times (i.e., picomolar- and nanomolar-responsive genes retained their dose sensitivity over time) (fig. S2). These results indicate that dose sensitivity is not time-dependent.

Different chromatin states at picomolar- and nanomolar-responsive ERα enhancers

To better understand the molecular mechanisms underlying the dose-dependent formation of ERα enhancers that direct the expression of estrogen target genes in response to E2, we determined the ERα cistrome in MCF-7 cells across a range of E2 concentrations by chromatin immunoprecipitation sequencing (ChIP-seq) (Fig. 2A and fig. S3A). We observed that a subset of the ERα cistrome formed at low (picomolar) concentrations of E2 and expanded at higher doses, with the sites of ERα binding at lower doses being a subset of those observed at higher doses (i.e., the ERBSs at higher doses encompass nearly all of those observed at lower doses; fig. S3, A and B). ERα bound the "low-dose" enhancers at 10 pM E2 to the same extent that it bound to the "high-dose" enhancers at 10 nM E2 on the basis of average read counts for each class (Fig. 2, B and C). On the basis of these analyses, we also defined the doses at which genomic sites first became accessible to ERα binding.

In subsequent analyses, we assayed additional features associated with ERBSs, including chromatin accessibility [by assay for transposase-accessible chromatin using sequencing (ATAC-seq)] and H3K27ac enrichment (by ChIP-seq) (Fig. 2, D and E, and fig. S3, C and D). As with ERα binding, chromatin accessibility and H3K27ac enrichment were the greatest at sites that first exhibited ERα binding at the lowest doses of E2 (Fig. 2, D and E). Moreover, we observed that the low-dose (picomolar) ERBSs were more open, accessible, and active in the basal state (without E2 treatment) than the high-dose (nanomolar) sites (Fig. 2F; note that for these analyses, combined data from the 10 and 100 pM E2 treatment groups are designated pM* and combined data from the 1 and 10 nM E2 treatment groups are designated nM*; see table S2). These analyses included enhancer transcription data from precision run-on sequencing (PRO-seq) (Fig. 2F, right); enhancer transcription is a robust indicator of enhancer activity (*29*, *44*). Together, these results demonstrate that enhancers that form at ERBSs in response to low doses of E2 do so at accessible sites in the genome.

Significant ERα binding to DNA and chromatin at low doses of E2 occurs across a range of ERα concentrations

To determine whether ERα binding to chromatin at low doses of E2 occurs exclusively at the high levels of the receptor found in MCF-7 cells, we assayed binding in other breast cancer cell lines that express lower levels of ERα: T-47D and MDA-MB-361 cells, which have 50 and 10% of the levels of ERα found in MCF-7 cells, respectively, as determined by Western blotting (Fig. 3A). The estimated nuclear concentrations based on the literature and our Western blotting are as follows: MCF-7, 0.1 μM; T-47D, 0.04 μM; MDA-MB-361, 0.01 μM, representing a 10-fold range of ERα concentrations (see Materials and Methods). We performed ChIP-qPCR at two doses of E2 (10 pM and 10 nM) to determine whether "low-dose" ERBSs could be observed in T-47D and MDA-MB-361 cells. Our results indicate that in cells with twofold less (T-47D) or 10-fold less (MDA-MB-361) ERα than MCF-7 cells, robust ERα binding was detected at a selection of genomic loci (Fig. 3, B to D, and fig. S4). Thus, ERα binds to native chromatin at low doses of E2 across a range of ERα concentrations.

To address this in more detail across a greater range of ERα and E2 concentrations, we developed a computational model to explore the fractional occupancy of ERα on ERE DNA (see Materials and Methods). We used a steady-state equilibrium model that accounts for a multistep assembly of the active receptor complex as follows: ER + E2 ⇔ ER-E2 ⇔ 2(ER-E2) + ERE DNA ⇔ 2(ER-E2)-ERE DNA. The model is based on assumptions, parameters, and understanding of steroid hormone receptor activity supported by the literature. We collected values for all of the parameters used in the analysis from a minimum of two sources in the literature but typically more (see Materials and Methods). We plotted the fractional occupancy of ERα on DNA (θ) versus ERα concentration across a range of E2 concentrations (Fig. 3E) and with variations in the constants used [dissociation constants (K_d's) for E2 binding to ERα, dimerization ERα, and ERα dimer binding ERE DNA] (table S3). These results demonstrate the potential of low doses of E2 to drive ERα occupancy on DNA even at physiological levels of the receptor, such as those found in rodent myometrium, a classical estrogen-responsive tissue (Fig. 3F). Collectively, these results demonstrate that while ERα concentration influences ERα occupancy on DNA, significant ERα binding at low doses of E2 occurs even at low concentrations of the receptor.

Different FOXA1 and GATA3 usage at picomolar- and nanomolar-responsive ERα enhancers

The efficient formation of ERα enhancers requires cooperation with FOXA1 and GATA3, which have been described as "pioneer factors" for ERα (*30*, *31*, *35*, *54*–*56*). To determine whether picomolar- and nanomolar-responsive ERα enhancers might use FOXA1 and GATA3 differently, we performed a de novo motif analysis in the vicinity of ERBSs. We observed a significant enrichment of the canonical palindromic ERE, with the greatest enrichment in the enhancers established at 10 pM E2 (Fig. 4, A to C). A similar analysis revealed significant enrichment of FOXA1 motifs at ERBSs, also with the greatest enrichment in the enhancers established at 10 pM E2 but with a precipitous reduction for enhancers formed at higher

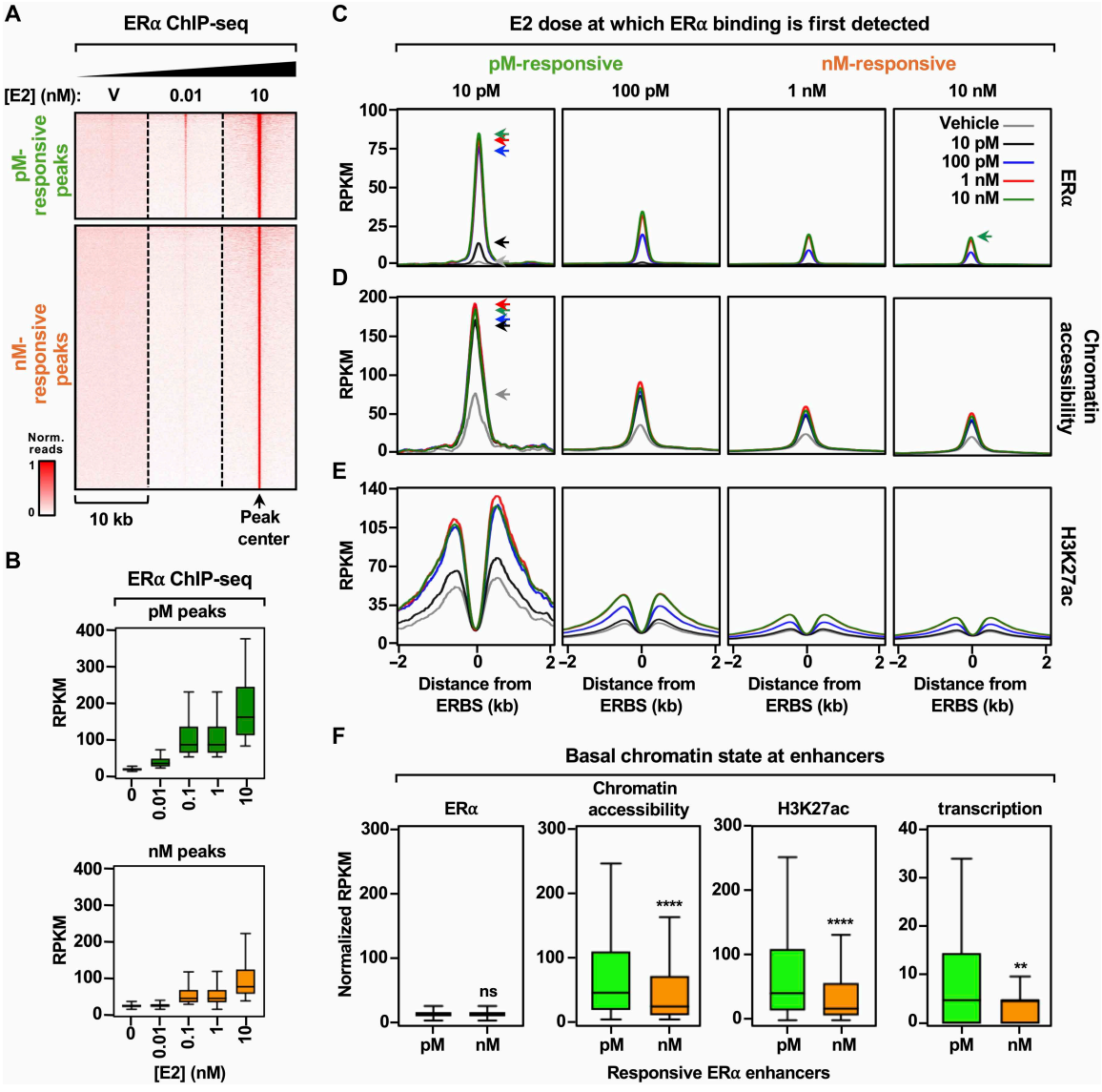

Fig. 2. Analysis of chromatin state at picomolar-responsive and nanomolar-responsive ERα enhancers. (**A**) Heatmap showing ERα binding across the genome as determined by ChIP-seq after 60 min of treatment with vehicle (DMSO), 10 pM E2, or 10 nM E2. ERBS groups are labeled in aggregate as picomolar peaks (1 to 100 pM E2) and nanomolar peaks (1 to 100 nM E2). (**B**) Box plots showing ERα read counts at picomolar-responsive (top) and nanomolar-responsive (bottom) ERBSs for a range of E2 concentrations. (**C** to **E**) Metaplots showing the read counts in RPKM around ERBSs from genomic assays over a range of E2 concentrations (10 pM to 10 nM). (C) ERα binding by ChIP-seq, (D) chromatin accessibility by ATAC-seq, and (E) H3K27ac enrichment by ChIP-seq. Peaks are centered on the summits of significant ERBSs. (**F**) Box plots showing the normalized read counts for ERα binding (ChIP-seq), chromatin accessibility (ATAC-seq), H3K27ac enrichment (ChIP-seq), and transcriptional activity (PRO-seq) at picomolar-responsive and nanomolar-responsive ERBSs before E2 treatment. Wilcoxon rank-sum test; ns, not significant; $^{**}P < 5 \times 10^{-10}$, $^{****}P < 5 \times 10^{-15}$.

doses (Fig. 4, A to C). In contrast, GATA3 motifs showed the greatest enrichment at ERBSs established at higher doses of E2 (Fig. 4, A to C).

To explore this in more detail, we examined the binding of ERα to bulk chromatin at different doses of E2 with or without small interfering RNA (siRNA)–mediated knockdown of *FOXA1* and *GATA3*. Depletion of FOXA1 and GATA3 was confirmed by Western blotting (fig. S5A). As with the motif enrichment, we observed a greater enrichment of FOXA1 in bulk chromatin at 10 pM E2 than at 10 nM E2, and vice versa for GATA3 (fig. S5A). As expected, depletion of FOXA1 or GATA3 impaired ERα binding, with the effects of GATA3 most pronounced at 10 nM E2 (fig. S5A). Similar results were observed in locus-specific ChIP-qPCR assays for a collection of nine ERα enhancers and their target genes, expressed in aggregate (Fig. 4, D and E).

Additional genome-wide assays reinforced this conclusion. FOXA1 and GATA3 ChIP-seq at 10 pM and 10 nM E2 showed thousands of significant peaks for both factors across the genome in both conditions, many of which overlapped ERBSs (Fig. 5A and fig. S5B). Treatment with 10 pM E2 promoted the greatest enrichment of FOXA1 at ERBSs, whereas 10 nM E2 promoted the greatest enrichment of GATA3 (Fig. 5B and fig. S3C), with a significantly greater GATA3/FOXA1 ratio for the nM* dosage group (fig. S5D). The expansion of GATA3 across the ERα cistrome at the highest doses of E2 was evident in a Venn diagram plotted versus ERα binding at the various

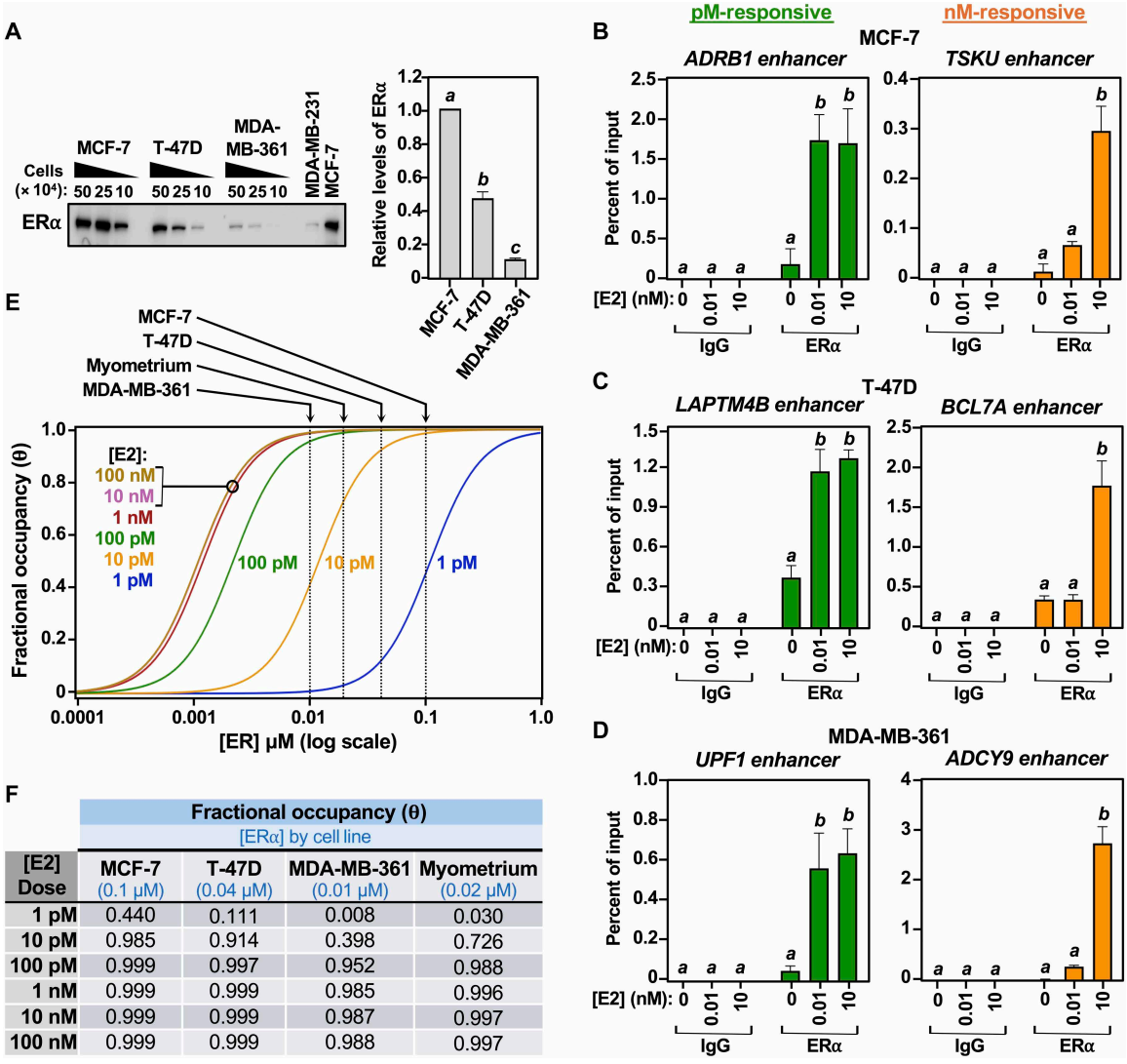

[E2] Dose	Fractional occupancy (θ) [ERα] by cell line			
	MCF-7 (0.1 μM)	T-47D (0.04 μM)	MDA-MB-361 (0.01 μM)	Myometrium (0.02 μM)
1 pM	0.440	0.111	0.008	0.030
10 pM	0.985	0.914	0.398	0.726
100 pM	0.999	0.997	0.952	0.988
1 nM	0.999	0.999	0.985	0.996
10 nM	0.999	0.999	0.987	0.997
100 nM	0.999	0.999	0.988	0.997

Fig. 3. Analysis of ERα binding to DNA and chromatin at low doses of E2 across a range of ERα concentrations. (**A**) Left: Western blot showing the relative concentrations of ERα across multiple ERα-expressing breast cancer cell lines (MCF-7, T-47D, and MDA-MB-361). Volumes of extract were loaded as serial dilutions representing 50×10^4, 25×10^4, and 10×10^4 cells for each cell line. MDA-MB-231 cells were used as a negative control. Right: Quantification of the results shown in the blot to the left. Values were normalized to ERα concentrations in MCF-7 cells. Each bar represents the mean + SEM; $n = 3$. Bars marked with different letters are significantly different from each other; one-way ANOVA, $P < 0.005$. (**B** to **D**) Bar graphs showing ERα ChIP-qPCR data for low dose–responsive (green) or high dose–responsive (orange) enhancer regions across multiple cell lines: (B) MCF-7, (C) T-47D, and (D) MDA-MB-361. The cells were treated with DMSO, 10 pM E2, or 10 nM E2 for 30 min. The data were normalized to input. Each bar represents the mean + SEM; $n = 3$. Bars marked with different letters are significantly different from each other. One-way ANOVA with Tukey's multiple comparison; $P < 0.05$. (**E**) Line graph showing the predicted chromatin occupancy (θ) at different ERα and E2 concentrations. Dotted lines mark the ERα concentrations for various breast cancer cell lines (MCF-7, T-47D, and MDA-MB-361) and rodent myometrial cells based on intracellular ERα derived from previously published results for each cell line (see Materials and Methods). (**F**) Table showing the computed θ values for various cells types across a range of E2 concentrations.

doses (Fig. 5C). Last, we used rapid immunoprecipitation mass spectrometry (MS) of endogenous proteins [RIME (*57*); also known as ChIP MS] as an orthogonal approach to monitor the dose-dependent enrichment of FOXA1 and GATA3 to chromatin-bound ERα. We observed E2-dependent recruitment of ERα to chromatin, with similar enrichment at both 10 pM and 10 nM E2 (Fig. 5D, top). As with the ChIP-seq results, we observed the greatest enrichment of FOXA1 at the lower dose of E2 and the greatest enrichment of GATA3 at the higher dose of E2 (Fig. 5D, bottom). Thus, in multiple different assays, we observed similar results. Collectively, our results indicate different FOXA1 and GATA3 usage at picomolar- and nanomolar-responsive ERα enhancers, with FOXA1 required for enhancer formation and target gene expression at low-dose enhancers and genes and GATA3 required at high-dose enhancers and genes.

Different modes of chromatin accessibility mediated by FOXA1 and GATA3 proximal to ERBSs

To better understand the differential usage of FOXA1 and GATA3 at picomolar- and nanomolar-responsive ERα enhancers, we considered the location of EREs relative to open regions of chromatin, as

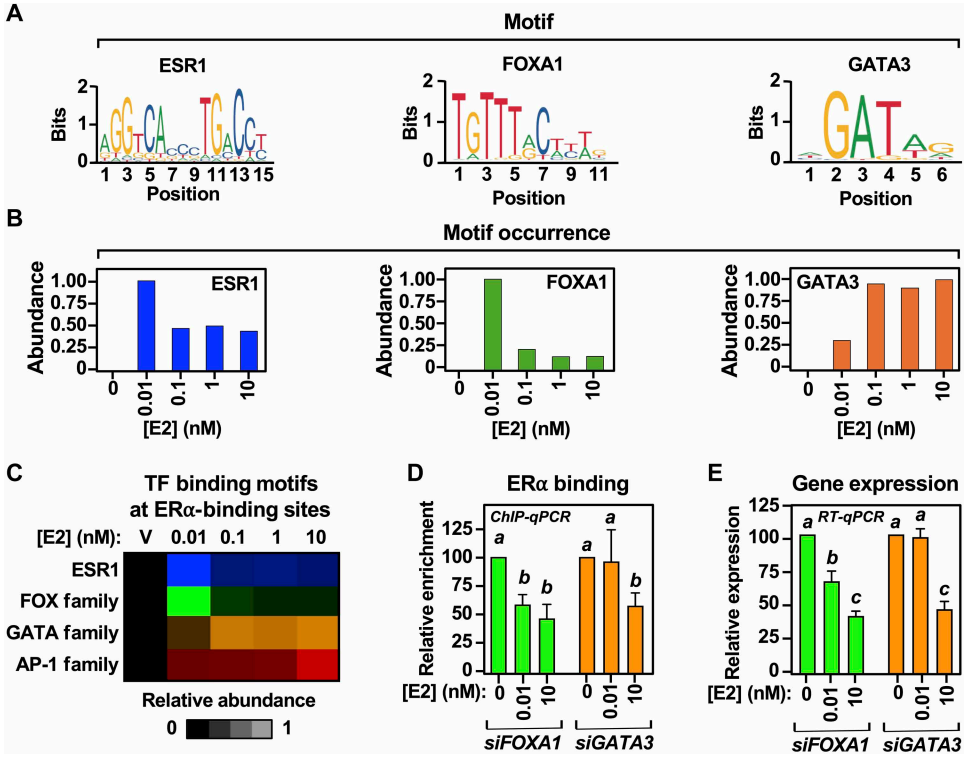

Fig. 4. Dose-dependent enrichment of FOXA1 and GATA3 motifs near ERBSs. (**A**) JASPAR gene logos of ESR1, FOXA1, and GATA3 motifs found ±200 bp around ERBSs. (**B**) Bar graphs showing the abundance of motif occurrences around ERBSs established over a range of E2 concentrations, normalized to their respective maximum values. (**C**) Heatmap showing the relative occurrences of ESR1, FOX family (FOXA1, FOXA2, and FOXO1), GATA family (GATA3, GATA4, and GATA6), and AP-1 family (FOS, c-JUN, ATF2, and ATF3) motifs over a range of E2 concentrations, normalized to their respective maximum values. (**D** and **E**) Effects of FOXA1 or GATA3 depletion by siRNA-mediated knockdown on (D) ERα binding to chromatin after 60 min of E2 treatment and (E) E2-dependent gene expression after 2 hours of E2 treatment. Bar graphs showing (D) relative enrichment from ERα ChIP-qPCR and (E) gene expression from RT-qPCR for E2-responsive enhancers and their cognate target genes. The data are expressed in aggregate for a collection of ERBS and target genes (*TFAP2C*, *TSKU*, *GREB1*, *MBOAT1*, *MIDEAS*, *CYP1B1*, *WNT16*, *ADRB1*, and *PGR*). The data are normalized to the control siRNA. Each bar represents the mean + SEM; $n = 3$. Bars marked with different letters are significantly different from each other. One-way ANOVA with Tukey's multiple comparison, $P < 0.05$.

determined by ATAC-seq. We began by inspecting examples of picomolar- and nanomolar-responsive enhancers: *XBP1* and *PGR*, which exhibit ERα binding at 10 pM and 10 nM E2, respectively (Fig. 6A). We observed that *XBP1* had four EREs in open regions of chromatin established by FOXA1 before E2 treatment, while *PGR* had none (Fig. 6B). The *PGR* enhancer, however, gained two newly available EREs only after treatment with E2. This suggests that ERα binding occurs in the presence of E2 when EREs are available in an accessible region of chromatin; this occurs before E2 treatment for FOXA1 and after E2 treatment for GATA3. This is observed globally, as treatment with E2 increases the total number of EREs in accessible regions across the genome (Fig. 6C).

We also observed that the distance between ERα and FOXA1 binding sites is associated with dose dependency. While ERBSs at picomolar-responsive enhancers are generally in close proximity to FOXA1 binding sites [mean of 740 base pairs (bp)], ERBSs at nanomolar-responsive enhancers are nearly threefold further away from FOXA1 binding sites (mean of 1915 bp) (Fig. 6D). In contrast, we observed little difference in the distance between ERBSs and GATA3 binding sites between picomolar- and nanomolar-responsive enhancers (Fig. 6D). In addition, regions of open chromatin near GATA3 binding sites showed a significantly larger increase in accessibility upon E2 treatment compared to FOXA1 binding sites, which showed a more modest increase in accessibility (Fig. 6E). Next, we investigated patterns of TF binding at initially accessible (before E2 treatment) and newly accessible (after E2 treatment) regions. In agreement with the results described above, we found that while ERα bound at initially open regions of chromatin in response to both picomolar and nanomolar E2 treatments, only nanomolar E2 treatment promoted ERα binding at newly opened regions of chromatin (Fig. 6F). This likely occurs because these regions are not yet sufficiently open at picomolar doses of E2.

Together, our results indicate that FOXA1 initially establishes open regions of chromatin accessible to ERα at low (picomolar) doses of E2, while GATA3 drives newly opened regions of chromatin after E2 induction in proximity to FOXA1 binding sites. These open regions of chromatin facilitate ERα binding if an ERE is present. With E2 treatment, larger regions become accessible, allowing ERα binding at sites farther away from the initial regions established by FOXA1.

AP-1 actions at ERα enhancers occur at high doses of E2

Previous studies have suggested that the TF activator protein 1 (AP-1) (Fos/Jun heterodimers) may also be enriched at ERBSs and may, in some cases, tether ERα to chromatin without the direct binding of the receptor to DNA (*31*, *32*, *58*, *59*). These analyses were performed with high (>10 nM) E2 treatment. When mining our data, we observed the greatest enrichment of AP-1 motifs at ERBSs established at the highest dose of E2, which exhibit lower enrichment of

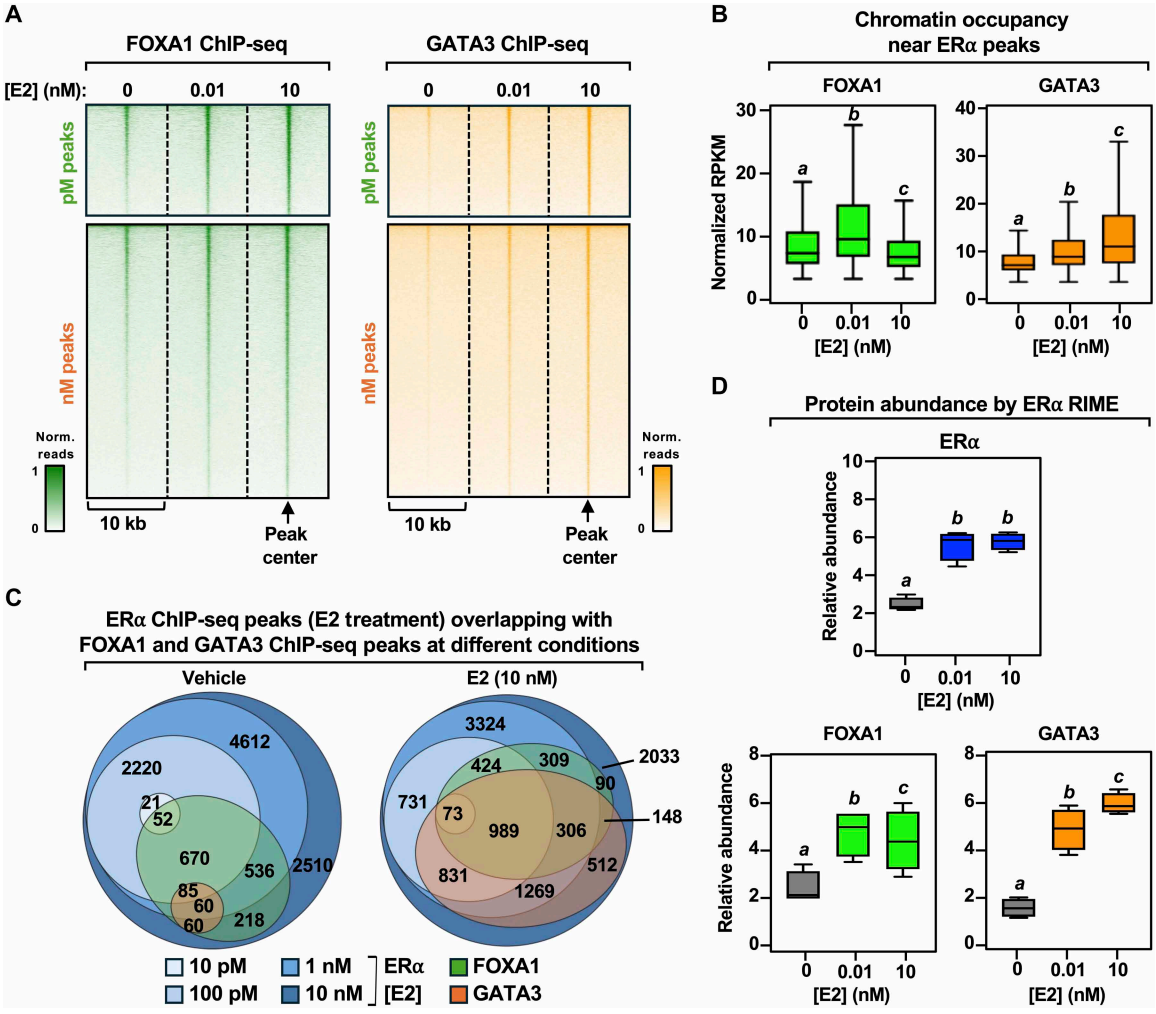

Fig. 5. Dose-dependent binding of FOXA1 and GATA3 at ERBSs. (**A**) Heatmap showing FOXA1 (left) and GATA3 (right) chromatin occupancy as determined by ChIP-seq for vehicle (V), 10 pM E2, and 10 nM E2 treatments at picomolar-responsive and nanomolar-responsive ERBSs. (**B**) Box plots showing the binding of FOXA1 (left) or GATA3 (right) at ERBSs in response to low (10 pM) and high (10 nM) E2 treatment. Bars marked with different letters are significantly different from each other. Wilcoxon rank-sum test, $P < 5 \times 10^{-10}$. (**C**) Euler diagrams showing overlaps of ERα ChIP-seq peaks across different E2 treatment concentrations (10 pM to 10 nM) with FOXA1 and GATA3 peaks after treatment with vehicle (left) or 10 nM E2 (right). Both Euler plots (left and right) show the binding of ERα by ChIP-seq across a range of E2 concentrations (10 pM, 100 pM, 1 nM, and 10 nM; blue-shaded circles with the key below the plots). These plots are superimposed with the FOXA1 and GATA3 ChIP-seq data obtained from cells treated with vehicle (left plot) or 10 nM E2 (right plot), as indicated by the labeling above the plots. (**D**) Box plots showing the relative abundance of FOXA1 and GATA3 associating with chromatin-bound ERα in response to low (10 pM) and high (10 nM) E2 treatment as determined by RIME. The data are normalized to the respective IgG controls. Bars marked with different letters are significantly different from each other. One-way ANOVA with Tukey's multiple comparison, $P < 0.05$.

EREs (10 nM; Fig. 4C and fig. S6A). A comparison of published c-Fos ChIP-seq data with our ERα ChIP-seq data showed the greatest enrichment of c-Fos at ERBSs established with the highest doses of E2 (fig. S6, B and C), suggesting that AP-1 actions at ERα enhancers, especially those lacking an ERE, may be a pharmacological response. Previous genomic studies found a strong negative correlation between ERE and AP-1 motifs (*31*), also hinting at the types of observations that we have made here.

Distinct RNA Pol II–dependent mechanisms at picomolar- and nanomolar-responsive promoters

We previously showed that E2-regulated genes, in aggregate, exhibit hormone-dependent loading of RNA Pol II [i.e., preinitiation complex (PIC) formation] and promoter-proximal Pol II pausing (*28*), which represent distinct mechanisms of gene regulation (*60*). To determine whether promoters responsive to picomolar or nanomolar concentrations of E2 might exhibit distinct Pol II–dependent mechanisms of gene regulation, we examined PIC formation and Pol II pausing by PRO-seq at representative examples of picomolar-responsive (e.g., *ADRB1*) and nanomolar-responsive (e.g., *PGR*) genes. These genes showed clear and distinct Pol II dynamics, with *ADRB1* exhibiting paused Pol II in the absence of E2, transitioning into elongating Pol II with 10 pM or 10 nM E2 (Fig. 7A, left). In contrast, *PGR* exhibited an absence of Pol II in the absence of E2, with loading and pausing of Pol II at 10 pM E2, and additional pausing and a transition into elongating Pol II at 10 nM E2 (Fig. 7A, right). These same trends were observed on a global scale, looking across all genes in each dosage group (Fig. 7B). The picomolar-responsive genes showed a greater

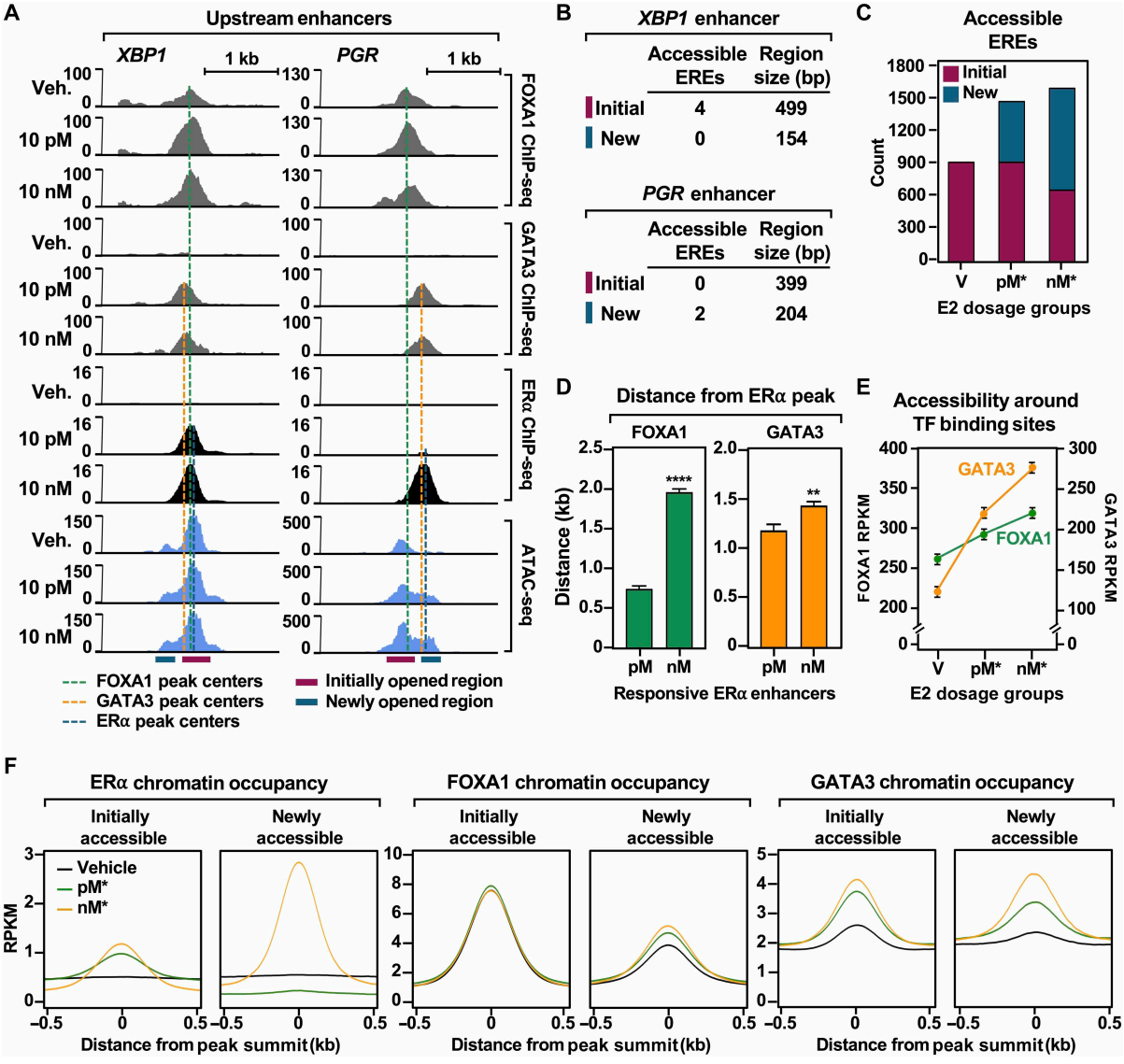

Fig. 6. ERα binding at picomolar-responsive enhancers occurs in open chromatin, while binding at nanomolar-responsive enhancers occurs at newly opened regions. (**A**) Browser tracks for upstream enhancer regions of representative picomolar-responsive (*XBP1*) and nanomolar-responsive (*PGR*) genes showing FOXA1, GATA3, and ERα ChIP-seq data with ATAC-seq data. Dotted lines highlight peak summits for FOXA1 (green), GATA3 (orange), and ERα (blue). Highlights below the tracks show regions that are open before (maroon) or after (dark blue) E2 induction as determined by ATAC-seq. (**B**) Table showing the number of ERE occurrences and length (in bp) of initially or newly open regions near the *XBP1* and *PGR* genes from (A) as determined by FIMO with a *P* value cutoff of <0.005. (**C**) Bar graphs showing the total number of ERE occurrences in open regions of chromatin that were available before (maroon) or after (dark blue) E2 treatment shown for two different dosage groups (pM = 1, 10, and 100 pM; nM = 1, 10, and 100 nM). (**D**) Bar graphs showing that average distances between ERα and FOXA1 (green) or GATA3 (orange) ChIP-seq peak summits within a 2-kb range for picomolar-responsive and nanomolar-responsive ERBSs. Each bar represents the mean + SEM. Student's *t* test, $^{**}P < 0.001$, $^{****}P < 0.0001$. (**E**) Line graphs showing chromatin accessibility around FOXA1 or GATA3 peaks from ChIP-seq for two different E2 dosage groups. Each point represents the mean ± SEM. (**F**) Metaplots of ERα, FOXA1, and GATA3 chromatin occupancy as determined by ChIP-seq within regions of accessible chromatin before (left) and after (right) E2 treatment as determined by ATAC-seq.

accumulation of reads in the promoter region [transcription start sites (TSSs) to +500 bp] before E2 treatment, as well as a higher pausing index (reads in the paused regions/gene body reads) (Fig. 7C). Moreover, the picomolar-responsive genes showed a decrease in the pausing index with the lowest doses of E2, whereas the nanomolar-responsive genes showed an increase in the pausing index at higher doses (Fig. 7D).

Integration of genomic data from picomolar- and nanomolar-responsive ERα enhancers and their corresponding target gene promoters reveals a clear dose shift for the genomic features assayed herein (fig. S7). It also showed that enhancer transcription, measured by PRO-seq, exhibits similar dose sensitivity as target gene transcription, again with a rightward dose shift for the nanomolar-responsive genes (fig. S7). Following these analyses, we explored additional aspects of enhancer transcription and enhancer RNA (eRNA) production in more detail. We previously showed that some eRNAs produced from ERα enhancers are enriched with functional eRNA regulatory motifs (FERMs) (Fig. 7E) that bind co-regulators

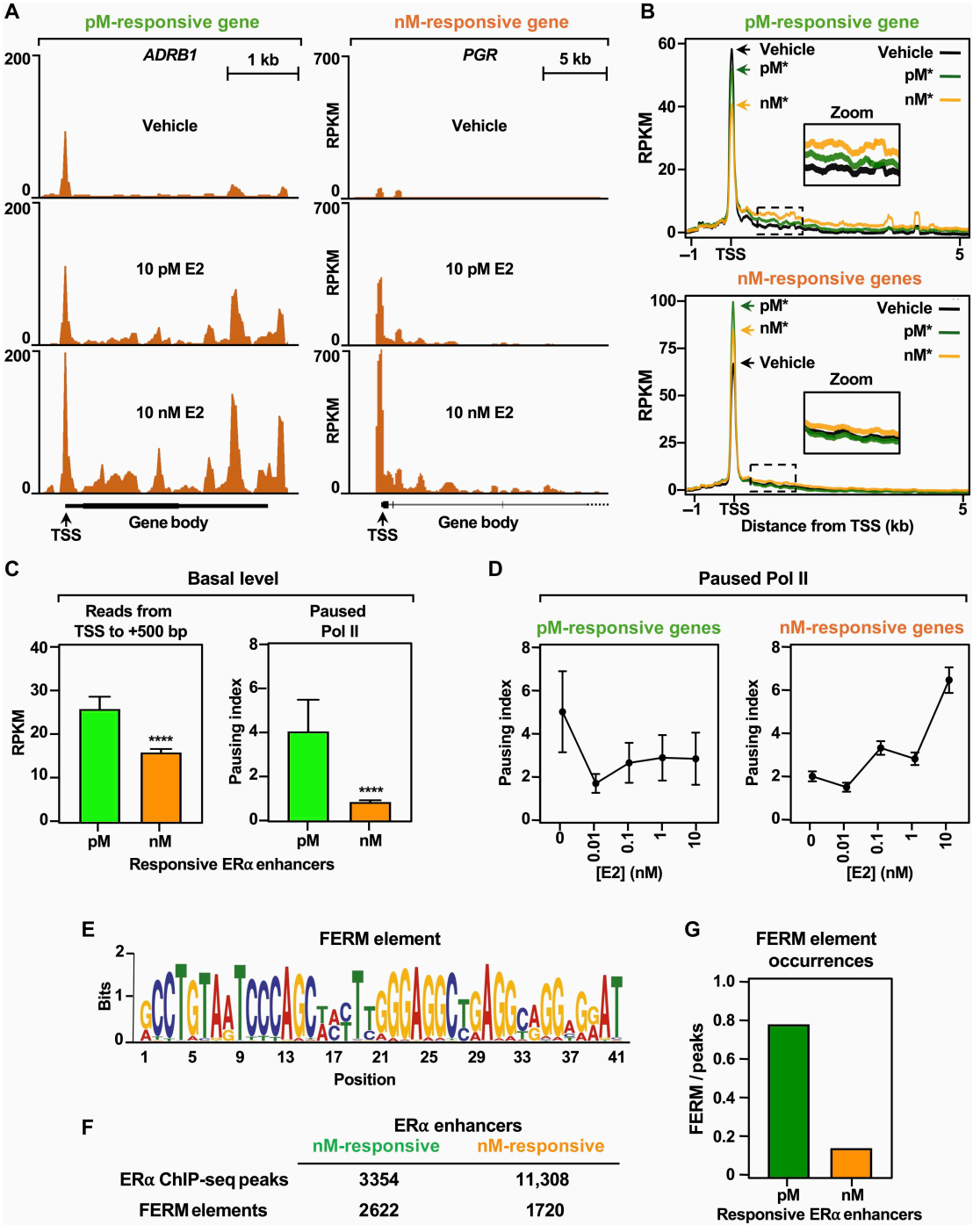

Fig. 7. RNA Pol II pausing and PIC formation at the promoters of picomolar-responsive and nanomolar-responsive genes. (**A**) Browser tracks showing representative genes in the picomolar-responsive (*ADRB1*) and nanomolar-responsive (*PGR*) gene groups. TSSs (arrows) and gene bodies are indicated for each gene. (**B**) Metaplots showing the average profile of PRO-seq data near the TSS and first 5 kb of the gene body for picomolar (top) and nanomolar (bottom) E2 dosage groups. Insets: Enlarged images of the regions indicated by a dashed box are shown to highlight transcription in the gene body. (**C**) Bar graphs showing read counts for TSS to +500 bp (left) and the pausing index (read counts at TSS/read counts in gene body; right) shown for picomolar-responsive and nanomolar-responsive genes before E2 treatment. Each bar represents the mean + SEM. Asterisks indicate significant differences; Wilcoxon rank-sum test, $****P < 5 \times 10^{-15}$. (**D**) Line graphs showing pause indexes across a range of E2 treatment concentrations for picomolar-responsive (left) and nanomolar-responsive (right) genes. Each point represents the mean ± SEM; $n = 1573$ genes for picomolar and $n = 2352$ genes for nanomolar. (**E**) Motif logo for the human FERM element. (**F**) Table showing the number of ERα peaks (ChIP-seq) and FERM element motif occurrences (FIMO) shown for picomolar-responsive and nanomolar-responsive ERBSs. (**G**) Bar graph showing the number of occurrences of FERM elements per number of ERα peaks shown for picomolar-responsive and nanomolar-responsive ERBSs.

and help establish transcriptionally active enhancers (*61*). We observed that FERMs are markedly enriched in the eRNAs produced from enhancers established in response to picomolar levels of E2 compared to eRNAs produced from enhancers established in response to nanomolar levels of E2 (Fig. 7F), especially when expressed as FERMs per ERBS (Fig. 7G). Together with the data from Figs. 1 and 2, these results show that the genes most highly responsive to low levels of E2 are regulated by ERα enhancers that form in open regions of chromatin and produce eRNAs enriched in FERMs and have promoters with low dose–responsive paused Pol II.

Differential co-regulator association with chromatin-bound ERα at picomolar and nanomolar doses of E2

To assess broadly how co-regulator recruitment to chromatin-bound ERα is affected by different doses of E2, we mined our ERα RIME data from experiments conducted at low (10 pM) and high (10 nM) concentrations of E2. We had good (58%) coverage of ERα peptides by MS in the RIME assays, indicating that the protocol was working well (Fig. 8A). As noted above, we observed E2-dependent recruitment of ERα to chromatin, with similar enrichment at both 10 pM and 10 nM E2 (Fig. 5D, top). We identified hundreds of proteins associating with chromatin-bound ERα, some with maximal association at 10 pM E2 (Fig. 8B) and others with maximal association at 10 nM E2 (Fig. 8C). Both sets of proteins were enriched for GO terms related to mRNA processing, splicing, and nucleosome assembly (Fig. 8, D and E). The classical ERα co-regulators p300 and NCOA3/SRC3 showed maximal (saturated) association with chromatin-bound ERα at 10 pM E2 (Fig. 8F), while NCOA2/SRC2 showed maximal (saturated) association with chromatin-bound ERα at 10 nM E2 (Fig. 8F). Comparison of our ERα RIME data with our previous MS data for FERM-interacting proteins (*61*) identified a set of proteins, many of which are involved in RNA processing and splicing, which may be associated with ERα enhancers in an E2 dose–dependent manner (fig. S8).

ERBSs are spatially organized into E2 dose–related TADs

To better understand how E2 dose–sensitive binding sites are spatially organized in the genome, we integrated high-throughput chromosome conformation capture (HiC) and ERα ChIP-seq data from MCF-7 cells. The TAD boundaries were stable across the treatment groups (vehicle, 10 pM E2, and 10 nM E2), yielding a consensus of 2991 TADs that were used for subsequent analysis (thus eliminating E2 dose as a variable for the TADs) (fig. S9A). The TADs were then categorized by the frequency of ERBS type (i.e., low dose or high dose). TADs with >70% of one type of ERBS were defined by that type, either pM* or nM*. TADs with a mixture of pM* and nM* ERBSs were categorized as mixed TADs, and TADs with no significant ERBSs were categorized as "no ERα" TADs (Fig. 9, A and B). A majority (65%) of the ERBS-containing TADs were highly enriched in a single ERα dosage category (Fig. 9A), with ERα binding (by ChIP-seq) reflective of the category (Fig. 9C). Figure 9D shows HiC contact maps to define TADs, aligned with ERα ChIP-seq and PRO-seq data for representative pM*, nM*, and "no ERα" TADs.

Additional analyses revealed that the ERBSs within the pM* TAD are spaced closer together on average (~70 kb on average) than those within nM* TADs (~80 kb) (Fig. 9E). Moreover, within the pM* and nM* TAD categories, the total transcriptional activity for all genes in the TAD (by PRO-seq) was maximum at the E2 concentrations corresponding to the categories (i.e., for the pM* TADs, the transcription levels were significantly higher at 10 pM E2 than 10 nM E2; Fig. 9F). Mixed TADs showed the total transcriptional activity directly proportional to the treatment dose, whereas the no ERα TADs showed a decrease in transcriptional activity with E2 treatment (Fig. 9F), suggesting a possible attenuation of transcription as the transcriptional machinery is recruited away to E2-regulated genes in the responsive TADs. As expected, on the basis of Fig. 7 (A to D), pM* TADs are enriched for genes with paused RNA Pol II at their promoters (fig. S9B). Together, these results show that the dose-dependent features of E2-responsive enhancers and genes are organized into TADs, forming spatially confined gene regulatory networks with distinct E2 dose sensitivities.

Poor outcomes of patients with breast cancer on aromatase inhibitor treatment is associated with picomolar-responsive ERα enhancers

To link enhancer formation with clinical outcomes, a previous study mapped the genome-wide chromatin-binding profiles of ERα in cancer samples from patients with breast cancer undergoing aromatase inhibitor treatment (Fig. 10A) (*62*). They characterized different binding patterns of ERα between patients with good or poor outcomes after aromatase inhibition and found that the ERα profiles predicted the treatment outcomes for first-line aromatase inhibitors (*62*). We overlaid their ERα ChIP-seq data from patient samples with our ERα ChIP-seq from MCF-7 cells (picomolar versus nanomolar peaks) (Fig. 10B). We observed that low-dose ERα enhancer usage was elevated in the samples from patients who have breast cancer with poor responses to aromatase inhibitors (Fig. 10C) with an expected elevated occurrence of FOXA1 motifs relative to GATA3 motifs (Fig. 10D). Given that patients who have breast cancer with poor outcomes on aromatase inhibitor therapy may experience incomplete reductions in circulating E2, our analyses suggest that the breast cancers in these patients may capitalize on the remaining E2 levels to promote enhancer formation at low dose–responsive ERBSs, leading to enhanced cancer cell growth. Collectively, our results identify mechanistic differences between low- and high-dose ERα enhancers that specify distinct biological outcomes.

DISCUSSION

In this study, we characterized the nonlinear sensitivity of the genomic and transcriptional landscape to varying E2 concentrations, revealing discrete regulatory states. By determining the molecular, genomic, and sequence features of ERα enhancers established over six orders of magnitude of E2 treatment, we were able to identify and characterize a class of ERα enhancers that are established and are active at low, physiological doses of E2 (1 to 100 pM). These "low-dose" enhancers are distinct from "high-dose" ERα enhancers established exclusively in the presence of high, pharmacological doses of E2 (10 to 100 nM) with respect to the molecular mechanisms, target gene sets, and biological outcomes. Our observations should be applicable across a range of steroid hormone–responsive biological systems. The implications of these findings are discussed in detail below.

Mechanisms of action and biological consequences of low-dose estrogen signaling

For most of a woman's adult life, exposure to E2 typically occurs at circulating levels in the picomolar range (typically ~100 pM up to 2 nM but frequently lower in prepubertal or postmenopausal females).

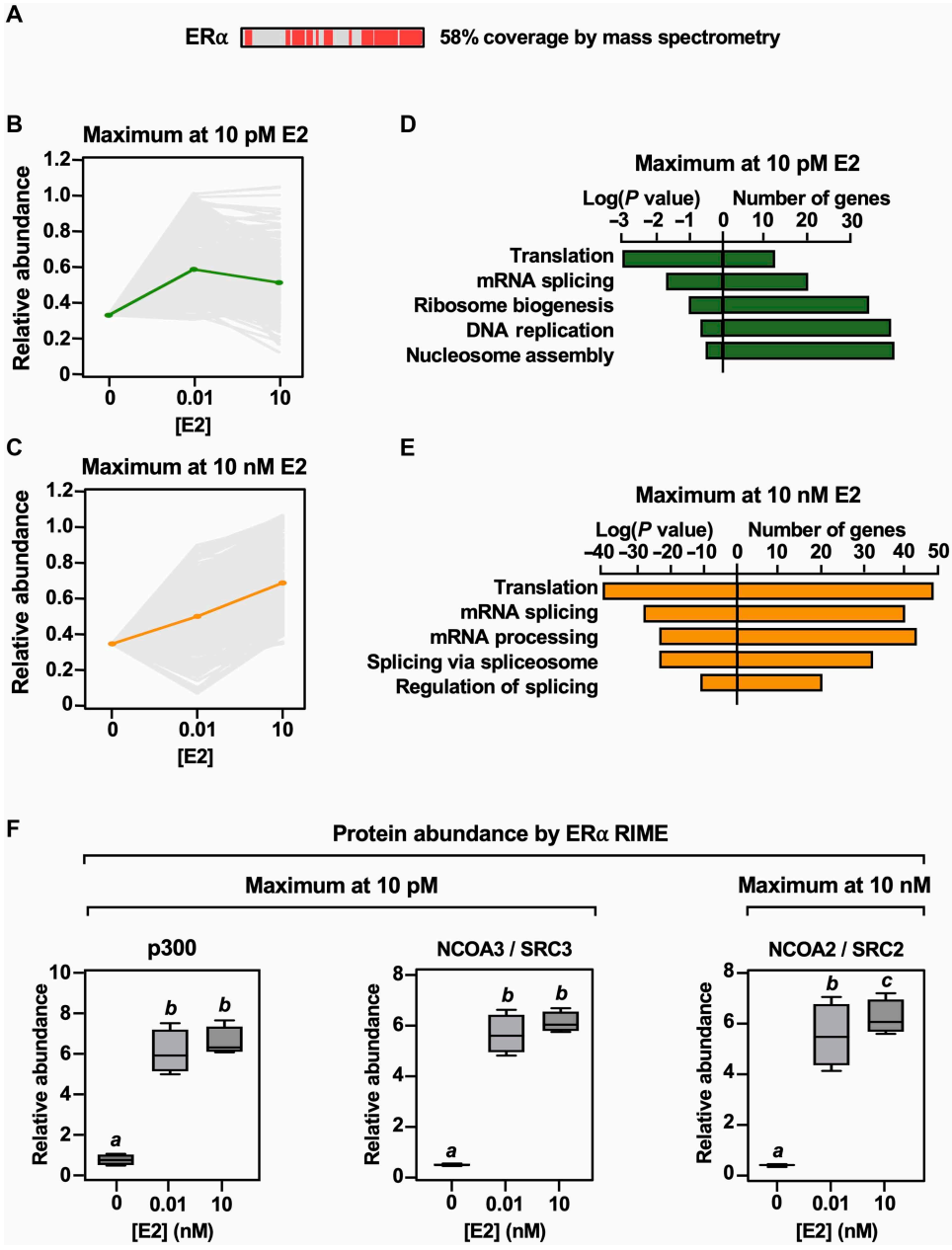

Fig. 8. ERα-RIME proteomic analysis showing protein abundance patterns for picomolar and nanomolar E2 treatments. (**A**) Coverage map from RIME MS data for ERα using the Sequence Coverage Visualizer web application. (**B** and **C**) Line graphs showing ERα-RIME data expressed as relative abundances for proteins with maximum enrichment at 10 pM E2 [(B), $n = 275$] or 10 nM E2 [(C), $n = 276$]. Gray lines show the enrichment values from individual proteins, while the colored lines show the average. (**D** and **E**) GO analysis showing the number of proteins and significance values for the top five terms from ERα-RIME data for proteins with maximum enrichment at 10 pM (D) or 10 nM (E) E2 treatment. (**F**) Box plots showing the relative abundance of co-regulators that associate with chromatin-bound ERα as determined by RIME. The abundances were normalized to the respective IgG controls. Representative proteins with maximum abundance at 10 pM E2 (p300 and NCOA3/SRC3) or 10 nM E2 (NCOA2/SRC2) are shown. Bars marked with different letters are significantly different from each other. One-way ANOVA with Tukey's multiple comparison, $P < 0.05$.

Much of what we know, however, about the genomic actions of E2 is from cell-based studies conducted at 10 to 100 nM E2. This has left a gap in knowledge about estrogen signaling and more broadly about steroid hormone signaling. Although a recent study examined ERα binding genome-wide over a range of E2 concentrations (1 pM to 10 nM) in breast cancer cells (*63*), it did not reveal the detailed molecular mechanisms uncovered herein. Another recent study using a zero-distance photocrosslinking assay coupled with MS in MCF-7 cells also assayed ERα binding to DNA over a range of E2 concentrations and determined an EC_{50} (median effective concentration) of 35 pM, providing an orthogonal demonstration of low-dose ERα binding in cells (*64*).

Our studies have defined the molecular features of picomolar- and nanomolar-responsive ERα enhancers and highlighted key

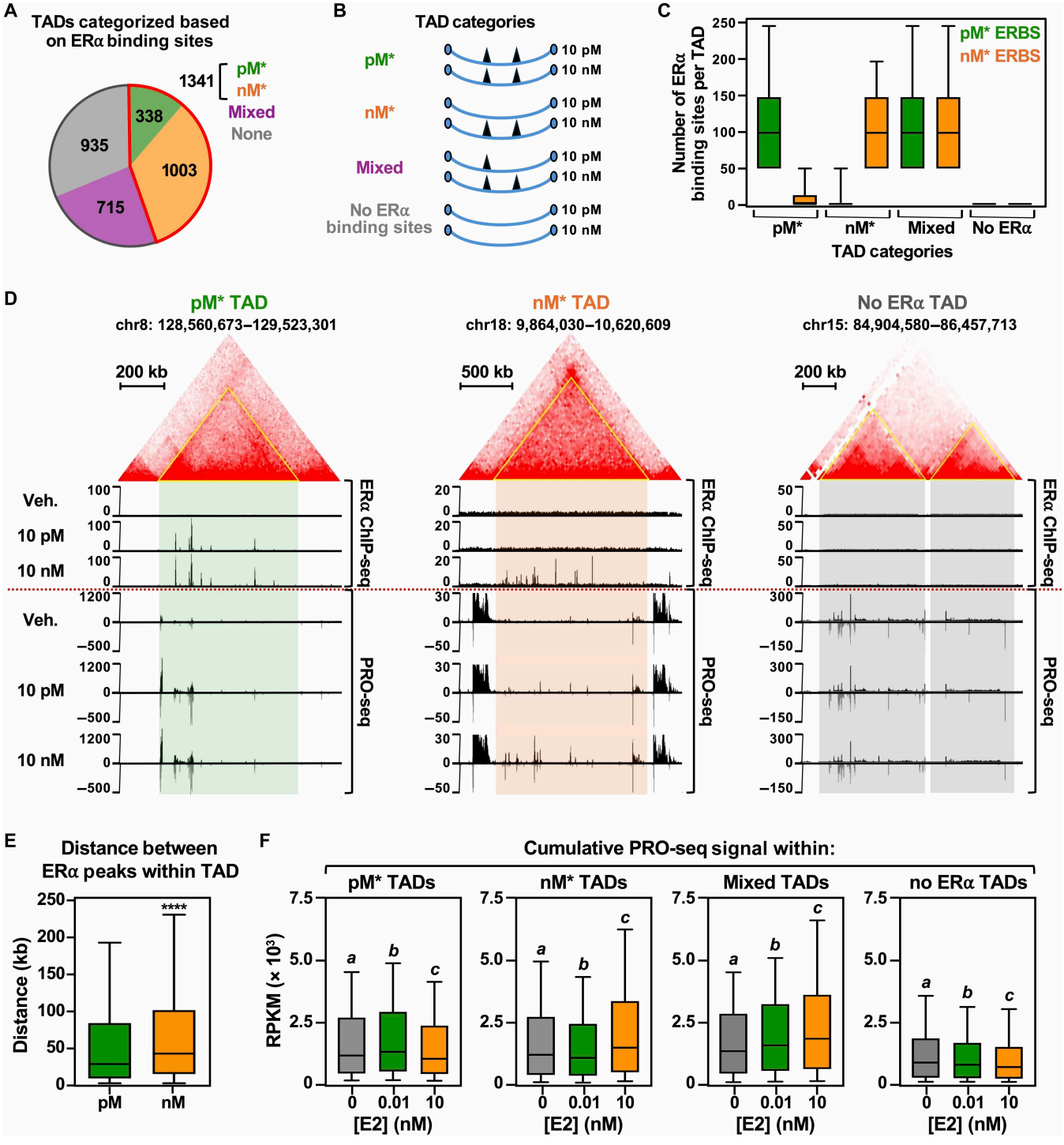

Fig. 9. ERBSs are spatially organized into E2 dose–related TADs. (**A**) Pie chart showing the proportion and number of TADs occupied by predominantly pM*, nM*, a mix of both pM* and nM*, or no ERBSs. (**B**) Schematic diagram showing the four TAD categories examined herein. (**C**) Box plots showing the number of pM* and nM* ERBSs within the TAD categories. (**D**) Contact maps (HiC) showing the interaction of genomic regions are presented with corresponding ERα ChIP-seq and PRO-seq browser tracks. TAD boundaries are highlighted in the contact maps with yellow lines. Representative data for a pM* TAD (left, green shading), a nM* TAD (middle, orange shading), and a "no ERα" TAD (right, gray shading). (**E**) Box plot showing the average distance between ERBSs within pM* or nM* TADs. Wilcoxon rank-sum test, ****$P < 5 \times 10^{-15}$. (**F**) Box plots showing the total transcription activity determined by PRO-seq and expressed in RPKM for each TAD category. Bars marked with different letters are significantly different from each other. Wilcoxon rank-sum test, $P < 5 \times 10^{-9}$.

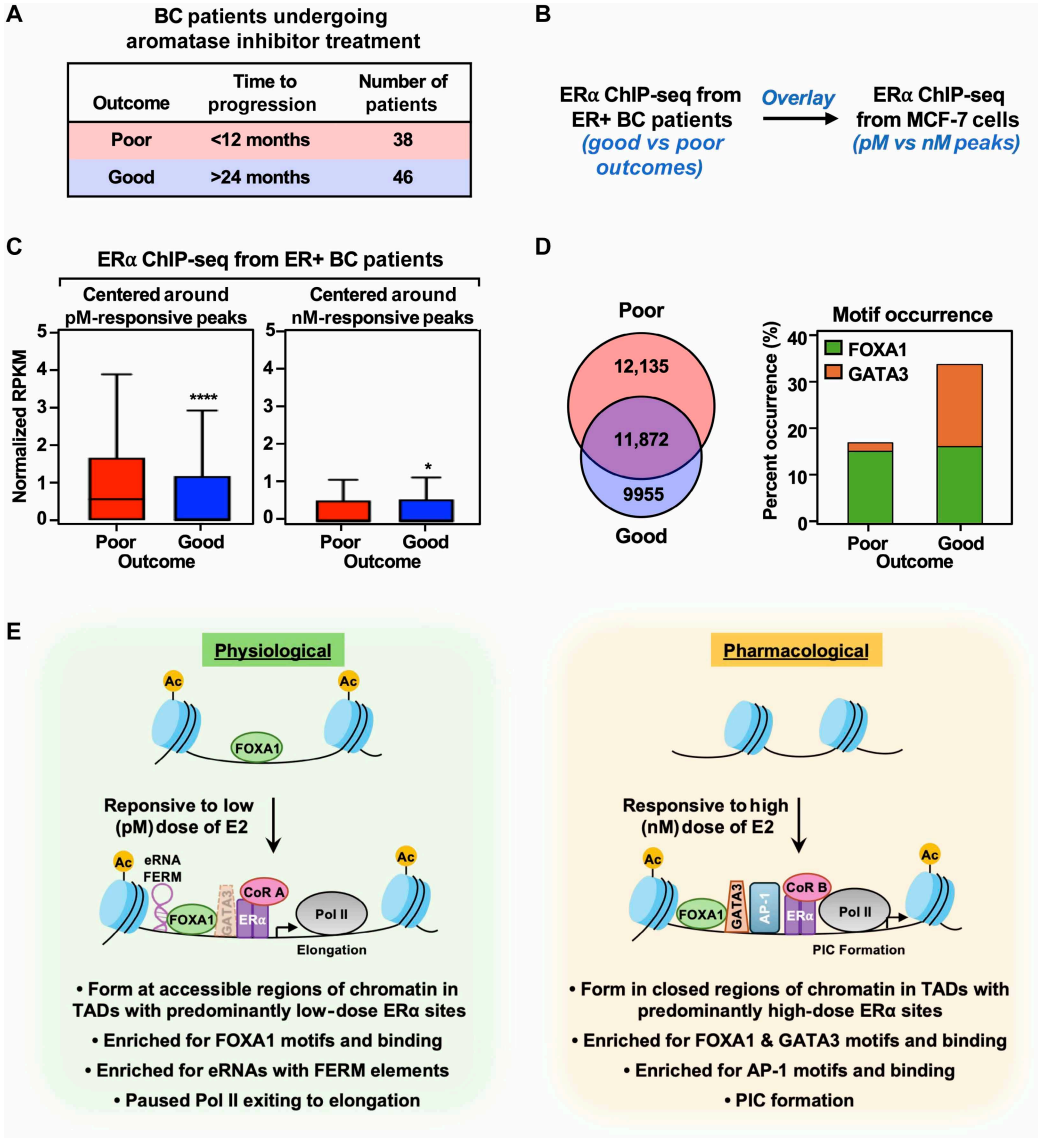

Fig. 10. Outcomes of patients with breast cancer on aromatase inhibitor treatment are associated with ERα binding at picomolar-responsive enhancers. (**A**) Table showing outcomes in 84 patients who underwent aromatase inhibitor treatment: Poor outcome (time to progression <12 months; highlighted in red) or good outcome (time to progression >24 months; highlighted in blue). Drawn from data presented in (*62*). BC, breast cancer. (**B**) Schematic diagram of analyses overlaying ERα ChIP-seq from patients with ER+ BC with ERα ChIP-seq from MCF-7 cells (picomolar versus nanomolar peaks). (**C**) Box plots showing ERα binding by ChIP-seq within picomolar-responsive (left) or nanomolar-responsive (right) ERBS for patients who have breast cancer with poor or good outcomes after aromatase inhibitor treatment. ChIP-seq data from patients with breast cancer (*62*) was mapped to the picomolar-responsive or nanomolar-responsive ERBS determined in MCF-7 cells. Asterisks indicate significant differences; Wilcoxon rank-sum test, $*P < 5 \times 10^{-5}$, $****P < 5 \times 10^{-15}$. (**D**) Venn diagram showing the number of overlapping peaks between patient outcome groups (left) and a graph showing the occurrence of FOXA1 or GATA3 motifs near the ERα enhancers in breast cancers from patients with poor or good outcomes (right). (**E**) Model showing the dose-dependent effects of E2 on gene regulation by ERα in breast cancer cells. See the text for details.

differences between the two (Fig. 10E). ERα in the presence of low, physiological concentrations of E2 binds preferentially to EREs located in open and accessible regions of chromatin prepared by FOXA1. Activation of these enhancers leads to the production of eRNAs containing FERM elements, as well as the subsequent activation of target gene promoters loaded with paused RNA Pol II. These genomic features are hallmarks of the most permissive regulatory element-gene pairs. Thus, physiological E2 signaling supports a gene regulation program with the lowest bar for activation. In contrast, high-dose, pharmacological E2 signaling requires GATA3 to open new, less tractable regions of chromatin, where ERα promotes the loading of RNA Pol II through PIC formation (Fig. 10F). ERBSs are spatially organized into E2 dose–related TADs, perhaps to facilitate coordinated responses to low doses of hormone.

Our analyses suggest that these distinctions can promote downstream biological outcomes. Cell growth and GO analyses indicate that different doses of E2 control biologically distinct outcomes, with low doses of E2 very effective in promoting proliferation in breast cancer cells (Fig. 1, D and E). As such, physiological, pathological, or therapeutic conditions with low circulating levels of E2 may experience

hormone-dependent gene expression profiles that specify distinct biological outcomes. For example, patients who have breast cancer with poor outcomes on aromatase inhibitor therapy may experience incomplete reductions in circulating E2. As our analyses suggest, the breast cancers in these patients may capitalize on the remaining E2 levels to promote enhancer formation at low dose–responsive ERBSs, leading to enhanced cancer cell growth (Fig. 10, C to E). Collectively, our results suggest that relevant biological outcomes that can be driven by low, subsaturating levels of hormone.

Considerations for the study of steroid hormone signaling

The advent of genomics over two decades ago led to the discovery of new facets of steroid hormone signaling and the molecular mechanisms of nuclear receptor function. ERα was the first nuclear receptor to be subject to genome-wide localization studies (*30*, *31*), with a set of standard conditions established early on and applied fairly consistently since then, including a high dose (typically 100 nM) of hormone. Under typical conditions, the fractional occupancy of ERα at 10 pM can exceed 50% (Fig. 3, E and F). As our results show, these subsaturating levels of E2 are sufficient to drive the biology of ERα and do so in a manner distinct from high, saturating doses of E2. Consequently, previous studies conducted at high E2 concentrations captured the combined effects of low and high doses, preventing clear differentiation of mechanisms occurring at different doses. In this regard, previous studies may have overemphasized the importance of GATA3 and AP-1 in physiological responses to E2.

A recent study examining the dose-dependent effects of androgens in androgen receptor (AR)–expressing cells reported observations different than ours with E2/ERα, likely reflecting differences between the cell biology of AR and ERα. Safi *et al.* (*65*) observed no significant binding of AR to chromatin by ChIP-seq at low doses of the synthetic androgen R1881 (10 and 30 pM) that elicited proliferative responses. This is in contrast to the significant binding of ERα to chromatin that we observed at 1 and 10 pM E2. On the basis of additional analyses, they concluded that low doses of androgens act through an AR monomer to promote nongenomic activation of the mechanistic target of rapamycin signaling pathway to drive proliferation. Only at higher doses do androgens promote the classical genomic effects of AR to drive an androgen-dependent transcriptional program (*65*). An important distinction between the E2/ERα and androgen/AR systems that is likely to underlie the differences at low doses of hormone is that ERα is nuclear in the absence of ligand, whereas AR is cytosolic and must translocate to the nucleus upon hormone exposure. These results highlight the need to evaluate steroid hormone signaling over a range of doses and explore a variety of potential molecular mechanisms.

Potential role of low dose–responsive ERα enhancers in the evolution of the estrogen response

Our work highlights the convergence of retrotransposons, regulatory elements, open chromatin, and transcriptional enhancers, with implications for the evolution of a signal-regulated transcriptional response. Many TF binding sites, including those for ERα, are located in Alu and related elements (*66*–*68*). In a previous study, we found the eRNA FERM element, which is encoded in Alu elements (humans) and B1 elements (rodents and other mammals), two types of retrotransposons belonging to the class of short interspersed nuclear elements (*61*). Isolated FERM RNAs are sufficient to drive E2-regulated target gene expression when artificially recruited to and tethered at native ERα enhancers (*61*). The combination of EREs and FERMs—two sequences that are hallmarks of low dose–responsive ERα enhancers—within Alu elements comprises a genetic element with the potential to mobilize and populate new regions of the human genome. This could allow for reorganization of the low-dose estrogen–responsive ERα cistrome and transcriptome, ultimately generating variability in the hormone response across the human population. Given that evolution is most likely to act in the context of physiological, rather than pharmacological, doses of E2, low dose–responsive ERα enhancers have the potential to shape the natural history and evolution of the estrogen response, as well as therapeutic responses that target the synthesis of E2 or the activity of ERα.

"Dose" as a driver of enhancer function and transcriptional regulation

Many aspects of transcriptional regulation are quantitatively encoded rather than all or none, with cells capable of sensing and interpreting the concentration or abundance of signaling molecules and effectors. Our studies on the effects of hormone dose in ERα-dependent transcriptional regulation provide a clear example of this. More broadly across the realm of enhancer-mediated gene regulation, the quantitative abundance of inputs such as ligands, TFs, and co-regulators have the potential to elicit dose-dependent effects that control gene expression outputs. For example, a recent study has shown that some regulatory elements are sensitive to the dosage of the TFs that control them (*69*). The results of another study suggest that TFs compete for limiting amounts of co-regulators, such as CBP, which exhibits haploinsufficiency (*70*), akin to a dose-dependent effect. As these types of analyses evolve, concepts related to dose sensitivity may be found to extend to posttranslational modifications, eRNAs, and nucleic acid–based motifs.

MATERIALS AND METHODS

Antibodies

The custom rabbit polyclonal antiserum raised against the first 113 amino acids of human ERα was generated in-house as previously described (*71*). Other antibodies used were as follows: FOXA1 (Abcam, ab23738; RRID: AB_2104842), GATA3 (Abcam, ab199428; RRID: AB_2819013), histone H3K27ac (Active Motif, 39133; RRID: AB_2561016), goat anti-rabbit HRP (horseradish peroxidase)–conjugated immunoglobulin G (IgG; Thermo Fisher Scientific, 31460; RRID: AB_228341), and rabbit IgG isotype control (Thermo Fisher Scientific, 10500C; RRID: AB_2532981).

Cell culture and treatments

MCF-7 cells (RRID: CVCL_0031) were provided by B. Katzenellenbogen (University of Illinois, Urbana-Champaign, Champaign, IL) and were maintained in minimal essential medium (Sigma-Aldrich, M1018) supplemented with 5% calf serum (Sigma-Aldrich, C8056), penicillin-streptomycin (100 U/ml; Gibco, 15140122), and gentamicin (25 μg/ml; Gibco, 1571004). MCF-7 cells were authenticated for cell-type identity using the GenePrint 24 system (Promega, B1870), blotting for ERα, and confirmed as mycoplasma-free every 6 months using the Universal Mycoplasma Detection Kit (American Type Culture Collection, 30-1012K). Fresh cell stocks were regularly replenished

from original stocks every few months (no more than 10 passages). For experiments involving estrogen treatment, the cells were grown for 3 days in phenol red–free Minimum Essential Medium Eagle (Sigma-Aldrich, M3024) supplemented with 5% charcoal-dextran–treated calf serum (CDCS; Sigma-Aldrich, C8056), 1 mM GlutaMAX (Gibco, 35050061), penicillin-streptomycin (100 U/ml; Gibco, 15140122), and gentamicin (25 μg/ml; Gibco, 1571004). All subsequent experiments involving E2 treatment were carried out in estrogen-free medium. For induction experiments, cells were treated with the indicated concentration of E2 (0 to 100 nM; Sigma-Aldrich, E8875) or dimethyl sulfoxide (DMSO) vehicle for the indicated experimental time.

Cell growth assays

MCF-7 cells were plated in phenol red–free minimum essential medium containing 5% CDCS for 72 hours before growth assays, as previously described (*72*). Cells were plated at a density of 20,000 cells per well in a six-well dish and treated with the indicated concentration of E2 for 5 days. Medium containing E2 was replenished every 2 days. At the experiment end point, the cells were trypsinized, and live cell count was obtained by staining with 0.4% trypan blue (Sigma-Aldrich, T8154) and counting using the Bio-Rad TC20 automated cell counter.

siRNA-mediated knockdown

siRNA-mediated knockdown was performed as previously described (*72*) using an SE Cell Line 4D-Nucleofactor X kit (Lonza; V4XC-1032; EEID: SCR_023155) according to the manufacturer's protocol. Briefly, MCF-7 cells were plated in phenol red–free minimum essential medium containing 5% CDCS. siRNAs targeting the mRNAs of interest or a control siRNA (Select Negative Control No. 1; Thermo Fisher Scientific, 4390843) were applied to MCF-7 cells at a final concentration of 30 nM in SE transfection reagent before electroporation using a Lonza 4D Nucleofector Nucleofection Transfection System Core Unit & X Unit with the CA 137 program. Cells were used for various assays 48 hours after siRNA transfection.

siRNA sequences

We used the following nucleic acid oligonucleotides for targeted knockdowns: siFOXA1_Hs01_00168403: 5′-CACACAAACCAAACCGUCA [dT][dT]-3′; siFOXA1_ Hs01_00168403_AS: 5′-UGACGGUUUGGUUUGUGUG [dT][dT]-3′; siGATA3_Hs01_00153931: 5′-CUCUGGAGGAGGAAUGCCA [dT][dT]-3′; siGATA3_Hs01_00153931_AS: 5′-UGGCAUUCCUCCUCCAGAG [dT][dT]-3′.

Preparation of cell extracts and Western blotting

Preparation of whole cell lysates

At treatment end points, the cells were washed twice with ice-cold 1× phosphate-buffered saline (PBS), scraped, and pelleted. The cell pellets were lysed in Lysis Buffer [20 mM tris-HCl, pH 7.6, 150 mM NaCl, 1 mM EDTA, 1% NP-40, 1% sodium deoxycholate, 0.1% SDS, 1 mM dithiothreitol (DTT), and 1× protease inhibitor cocktail (Roche, 11697498001)] by vortexing for >30 s. The lysate was cleared of debris by centrifugation at >20,000*g* for 15 min at 4°C. The supernatant containing the whole-cell extract was used for further analyses.

Subcellular fractionation

At treatment end points, the cells were washed twice with ice-cold 1× PBS, scraped, and pelleted. The cells were incubated with 100× packed cell volume (PCV) of Lysis Buffer (10 mM tris, pH 7.5, 60 mM KCl, 15 mM NaCl, 0.34 M sucrose, 2 mM EDTA, 0.5 mM EGTA, 0.1% Triton X-100, 650 μM spermidine, 1 mM DTT, and 1× protease inhibitor cocktail) for 10 min on ice. The cells were collected at 400*g* for 5 min, and the supernatant was collected as the cytoplasmic fraction. Pelleted nuclei were washed twice in excess Wash Buffer (10 mM tris, pH 7.5, 10 mM KCl, 0.34 M sucrose, 1.5 mM $MgCl_2$, 1 mM DTT, and 1× protease inhibitor cocktail). Pelleted nuclei were resuspended in 20× PCV of Nuclear Lysis Buffer (50 mM tris, pH 7.5, 140 mM NaCl, 1.5 mM $MgCl_2$, 0.5% NP-40, 1 mM DTT, and 1× protease inhibitor cocktail) for 20 min on ice, with occasional vortexing. Nuclear lysates were then cleared at >20,000*g* for 10 min at 4°C. The resulting supernatant was collected as the nucleoplasmic fraction. Pelleted chromatin was washed twice in excess Chromatin Buffer (10 mM Hepes, pH 8, 2 mM $MgCl_2$, 1% SDS, 1 mM DTT, and 1× protease inhibitor cocktail). The chromatin was then pelleted and resuspended in 2× PCV of Chromatin Buffer supplemented with universal nuclease (1 U/μl; Thermo Fisher Scientific, 88700). The resuspended material was then incubated for 1 hour at 37°C with shaking at 750 rpm in a thermomixer. The resulting material was used as the chromatin fraction.

Determination of protein concentrations and Western blotting

Protein concentrations were determined using a BCA (bicinchoninic acid) protein assay (Pierce, 23225). Aliquots of extract for analysis by SDS–polyacrylamide gel electrophoresis were mixed with 4× SDS Loading Solution (250 mM tris, pH 6.8, 40% glycerol, 0.04% bromophenol blue, 4% SDS, and 1% β-mercaptoethanol) to a final concentration of 1×. The samples were heated to 95°C for 5 min before separating by SDS–polyacrylamide gel electrophoresis and transferring to nitrocellulose membranes. The membranes were blocked using 5% nonfat milk in tris-buffered saline with Tween 20 for 30 min and incubated with the indicated primary antibody in tris-buffered saline with Tween 20 overnight at 4°C, followed by incubation with goat anti-rabbit HRP-conjugated IgG (1:5000 dilution). The washed blots were treated with ECL (enhanced chemiluminescence) detection reagent (Thermo Fisher Scientific, 34077, 34095) and visualized using a Bio-Rad ChemiDoc system at multiple exposure times.

Reverse transcription quantitative PCR (RT-qPCR)

MCF-7 cells were subjected to E2 dose treatments as described above and collected at the indicated experimental time point. For the RT-qPCR assays, cells were treated with E2 at the indicated dose for 2 hours. Total RNA was isolated using the QIAGEN RNeasy Plus Mini Kit (Qiagen, 74136) according to the manufacturer's protocol. Total RNA was reverse transcribed using oligo(dT) primers and MMLV reverse transcriptase (Promega, M1705) to generate cDNA. The resulting cDNA pool was treated with 3 units of ribonuclease H (RNase H) (Enzymatics, Y9220L) for 30 min at 37°C and then analyzed by qPCR using a Roche LightCycler 480 system with SYBR Green detection and gene-specific primers (see list below). Target gene expression was normalized to the expression of glyceraldehyde-3-phosphate dehydrogenase (GAPDH) mRNA.

RT-qPCR primer sequences

We used the following nucleic acid oligonucleotides for qPCR: GAPDH-F: 5′-GTCTCCTCTGACTTCAACAGCG-3′; GAPDH-R: 5′-ACCACCCTGTTGCTGTAGCCAA-3′; PGR-F: 5′-ACCACGCACGTTCTGCTAAT-3′; PGR-R: 5′-TGGAGCACCTAAGAGGAGCA-3′; ADRB1-F: 5′-TTCCTGCCCATCCTCATGCACT-3′; ADRB1-R: 5′-GTAGAAGGAGACTACGGACGAG-3′; WNT16-F: 5′-TCGGAAACACCACGGGCAAAGA-3′; WNT16-R: 5′-GCGGCAGTCTACTGACATCAAC-3′; MBOAT1-F: 5′-GGTTTCCACAGCTTGCCAGAAC-3′;

MBOAT1-R: 5′-ACCAGTCATCCACAAGGCAGGT-3′; TSKU-F: 5′-AGTCGCTTGACCTCAGCCACAA-3′; TSKU-R: 5′-TCGTGAAGGCAGACACTGAGAC-3′; GREB1-F: 5′-GGTCTGCCTTGCATCCTGATCT-3′; GREB1-R: 5′-TCCTGCTCCAAGGCTGTTCTCA-3′; CYP1B1-F: 5′-GCCACTATCACTGACATCTTCGG-3′; CYP1B1-R: 5′-CACGACCTGATCCAATTCTGCC-3′; MIDEAS-F: 5′-GCACAAGCCATCAGTCATCGTC-3′; MIDEAS-R: 5′-CTGCTTTGGTTTCCGCACGGAA-3′; TFAP2C-F: 5′-CACCTGTTGCTGCACGATCAGA-3′; TFAP2C-R: 5′-AGGAGCGACAATCTTCCAGGGA-3′; WNT16-F: 5′-TCGGAAACACCACGGGCAAAGA-3′; WNT16-R: 5′-GCGGCAGTCTACTGACATCAAC-3′; PARD6B-F: 5′-GTTTCAACGGCCAATCCACTGC-3′; PARD6B-R: 5′-CTATGGTTGTCAGGACGCAATAC-3′; LAPTM4B-F: 5′-GCTGTGTTTGGAACTGCTACCG-3′; LAPTM4B-R: 5′-GCAGCACCATTCACAGTGGCAT-3′; P2RY2-F: 5′-CGAGGACTTCAAGTACGTGCTG-3′; P2RY2-R: 5′-GTGGACGCATTCCAGGTCTTGA-3′.

Sequencing data quality control

For all of the NextGen sequencing assays described below (RNA-seq, ChIP-seq, ATAC-seq, and PRO-seq), raw FASTQ files of the data were assessed for sequencing quality using FastQC (*73*). Quality metrics, such as total reads, correlation between replicates, per-base sequence quality, GC content, adapter content, and duplication levels, were evaluated across all samples to ensure data suitability for downstream analysis per the Encyclopedia of DNA Elements (ENCODE) Project standards (*74*).

RNA-seq and analysis

Generation of RNA-seq libraries and sequencing

At treatment end points, RNA-seq libraries were generated from two biological replicates per condition as previously described (*61*). Total RNA from MCF-7 cells treated as indicated was isolated using the Qiagen RNeasy Plus Mini kit (Qiagen, 74136) according to the manufacturer's protocol. mRNA was enriched using Oligo(dT)25 beads (Invitrogen, 61002), and strand-specific, single-end libraries were generated using unique Illumina barcodes with a final amplification of 13 cycles. Resulting libraries were subjected to quality control analyses, including assessment of yield by a Qubit fluorometer (Invitrogen, Q32851) and size distribution by the DNA ScreenTape system (Agilent Technologies, G2964AA, 5067-5584, and 506705603), and sequenced using an Illumina NextSeq 2000 by 100-bp single-end sequencing.

Analysis of RNA-seq data

FASTQ files were subjected to quality control analyses using the FastQC tool (*73*). The single-end RNA-seq reads were aligned to the human genome using TopHat version 2.0.12 (*75*), with genome indices built using Bowtie2 version 2.1.0 (*76*). Aligned bam files were used for downstream processing (*77*). Aligned reads were quantified using featureCounts from the Subread version 1.6.3 package (*78*). Gene-level read counts were obtained using the GENCODE version 35 GTF annotation, specifying exon-based counting (-t exon), strand specificity (-s 2), and fractional assignment of multimapped reads (--fraction). Gene counts were normalized and tested for differential expression using DESeq2 (*79*). Normalized counts were used for principal components analysis and hierarchical clustering. Pairwise comparisons between vehicle and each E2 dose were performed using the Wald test in DESeq2. Differentially expressed genes were defined by adjusted $P < 0.05$ and a fold change >1.5 (up-regulated) or <0.67 (down-regulated).

ChIP and ChIP-qPCR

Chromatin immunoprecipitation

ChIP was performed as previously described (*61*) with some modifications. MCF-7 cells were grown to ~80% confluence under conditions and with E2 treatments as described above. After treatment, the cells were cross-linked with 1% formaldehyde (Thermo Fisher Scientific, 28-906) in 1× PBS at 37°C for 10 min. The cross-linking was quenched with glycine at a final concentration of 125 mM for 5 minutes at 4°C. The cells were washed thoroughly with ice-cold 1x PBS and collected by scraping into 1 ml of ice-cold 1× PBS. The cells were pelleted by centrifugation and lysed by pipetting in Farnham Lysis Buffer (5 mM Pipes, pH 8, 85 mM KCl, 0.5% NP-40, 1 mM DTT, and 1× complete protease inhibitor cocktail). Nuclei were collected by brief centrifugation and resuspended in SDS Lysis Buffer (50 mM tris-HCl, pH 7.9, 1% SDS, 10 mM EDTA, 1 mM DTT, and 1× complete protease inhibitor cocktail) by pipetting and incubating on ice for 10 min.

The chromatin was sheared to ~200- to 500-bp DNA fragments by sonication using a Diagenode Pico sonication device (Diagenode, B01080010) for eight cycles of 30 s on/30 s off. The fragment size was verified by agarose gel electrophoresis before quantification of protein concentrations using a BCA protein assay kit (Pierce, 23225). The samples were diluted 10-fold using Dilution Buffer (20 mM tris-HCl, pH 7.9, 0.5% Triton X-100, 2 mM EDTA, and 150 mM NaCl) with freshly added 1 mM DTT and 1× protease inhibitor cocktail. Soluble chromatin (500 μg per reaction) was precleared with Protein A Dynabeads (Invitrogen, 10001D). Protein A Dynabeads were incubated with 10 μl of polyclonal antiserum for ERα or 5 μg of rabbit IgG control (Thermo Fisher Scientific, 10500C; RRID: AB_2532981) for 2 hours, washed with Dilution Buffer, and applied separately to precleared chromatin samples. The chromatin fractions and the antibody-loaded Protein A Dynabeads were incubated overnight at 4°C.

The immune complexes on the beads were washed once with each of the following Wash Buffers in order: (i) Low-Salt Wash Buffer (20 mM tris-HCl, pH 7.9, 2 mM EDTA, 125 mM NaCl, 0.05% SDS, 1% Triton X-100, and 1× complete protease inhibitor cocktail); (ii) High-Salt Wash Buffer (20 mM tris-HCl, pH 7.9, 2 mM EDTA, 500 mM NaCl, 0.05% SDS, 1% Triton X-100, and 1× complete protease inhibitor cocktail); (iii) LiCl Wash Buffer (20 mM tris-HCl, pH 7.9, 1 mM EDTA, 250 mM LiCl, 1% NP-40, 1% sodium deoxycholate, and 1× complete protease inhibitor cocktail); (iv) 1× tris-EDTA containing 1× complete protease inhibitor cocktail. The immune complexes precipitates were transferred to a new tube in 1× tris-EDTA before incubation in Elution Buffer (100 mM $NaHCO_3$ and 1% SDS) overnight at 65°C to decross-link and elute. Eluates were treated with DNase-free RNase (Roche, 11119915001) for 30 min at 37°C, followed by 50 μg of proteinase K (Life Technologies, 2542) for 2 hours at 55°C. Genomic DNA was purified by phenol chloroform extraction.

ChIP-qPCR

For ChIP-qPCR assays, MCF-7 cells were treated with the indicated concentration of E2 for 30 min. Chromatin-immunoprecipitated DNA was analyzed by qPCR as described for RT-qPCR above. Non-specific background signals were determined by performing ChIP using rabbit IgG. The data were expressed as a percentage of input or a relative enrichment versus control or background.

ChIP-qPCR primer sequences

We used the following nucleic acid oligonucleotides for ChIP-qPCR: PGR-enhancer-F: 5′-CACTTGTCACATTGGAGGCAG-3′;

PGR-enhancer-R: 5′-TGGGTCATCCTGTTCCCTTTG-3′; ADRB1-enhancer-F: 5′-AGGGCTGGTAGTTAGGAGGA-3′; ADRB1-enhancer-R: 5′-AGCTTTTCTATGGGAGATGTGCT-3′; WNT16-enhancer-F: 5′-GCTTTCCCCCAAGGTTGCTA-3′; WNT16-enhancer-R: 5′-CTCGGGACCTCAGGCTCTTA-3′; MBOAT1-enhancer-F: 5′-CTTCCAAACTCGCAAGCCAC-3′; MBOAT1-enhancer-R: 5′-CTCCAGCAGGAGTGAGTGTG-3′; TSKU-enhancer-F: 5′-TTCCCCGGAGTTTACTTGCC-3′; TSKU-enhancer-R: 5′-AAAGTCCTCTGACCCCCTGT-3′; GREB1-enhancer-F: 5′-TAGGCTTCAAGAGGACCACA-3′; GREB1-enhancer-R: 5′-AGCAGCAAAACTGCATAGGA-3′; CYP1B1-enhancer-F: 5′-CCGGGTTTTAAGGACTGGGT-3′; CYP1B1-enhancer-R: 5′-TGAAAGCCTGCTGGTAGAGC-3′; MIDEAS-enhancer-F: 5′-CCCAGAAGATCTGAGGGCAA-3′; MIDEAS-enhancer-R: 5′-ACATCCTGCCCAGTTTCCTC-3′; TFAP2C-enhancer-F: 5′-CCGTGACCCCGATTTTGGAT-3′; TFAP2C-enhancer-R: 5′-CCAGCTCACCTCGCAGTC-3′; THBS1-enhancer-F: 5′-CCGTGTCACTTGTCTGGTCA-3′; THBS1-enhancer-R: 5′-AGAAAAAGCGAGGCGAAGGA-3′; PCYT1A-enhancer-F: 5′-CTCGTGTTCCCTTAGGTCCG-3′; PCYT1A-enhancer-R: 5′-AATGCGAAACACGGTGACCT-3′; UPF1-enhancer-F: 5′-GGTCTCGGTATTCTGCCTCG-3′; UPF1-enhancer-R: 5′-AGGTCACCCTGGATACTCCC-3′; KAZN-enhancer-F: 5′-TGGCCGATGGTGTTAAGGTG-3′; KAZN-enhancer-R:5′-GGCCTGTAGATGTGTCACCC-3′; LAPTM4B-enhancer-F: 5′-GATGTGTGACCTGGATGTGT-3′; LAPTM4B-enhancer-R: 5′-CCTTCTAAGCACAAGTATCTAGCA-3′; PARD6B-enhancer-F: 5′-TCATTCCAGTTCATCCCTGGT-3′; PARD6B-enhancer-R: 5′-CACGGGTTTGCTTTCTGACC-3′; CASP7-enhancer-F: 5′-GAAGTGCTCAGTCTCTCCCG-3′; CASP7-enhancer-R: 5′-AATATTTGTTGTGCGCCCCC-3′; ADCY9-enhancer-F: 5′-TGGCATGCTCACCAATCAGT-3′; ADCY9-enhancer-R: 5′-TCCCAGGGTACATGCTCAGA-3′; BCL7A-enhancer-F: 5′-AGGAACATTCCGTGGCAGAG-3′; BCL7A-enhancer-R: 5′-GGGGTAGACAGTTCCGTTCC-3′; KRT73-enhancer-F: 5′-TAGGCAGTGAGTGGATCACG-3′; KRT73-enhancer-R: 5′-CCAACTCAGCAGTGGTAGCC-3′; IL10RA-enhancer-F: 5′-CCTGGCCAAGGGCTATTTGA-3′; IL10RA-enhancer-R: 5′-CATTCCTCAGTGGGCTGGTT-3′; FGFR2-enhancer-F: 5′-GGTGATGGGGTGTAGTGAGG-3′; FGFR2-enhancer-R: 5′-GCGCGTGTGTACCCTAAGT-3′.

ChIP-seq and analysis

Generation of ChIP-seq libraries and sequencing

ChIP-seq libraries were generated from two biological replicates for each condition. A total of 100 ng of chromatin-immunoprecipitated DNA, prepared as described above, was used for library generation, as described previously with few modifications (*61*). Sequencing adaptors were annealed as previously described (*61*), and the libraries were sequenced using an Illumina NextSeq 2000. At least two biological replicates were sequenced for each condition with a minimum of ~40 million raw reads per condition.

Analysis of ChIP-seq data

Raw ChIP-seq reads were adapter trimmed using cutadapt version 1.9.1 (*80*) and aligned to the hg38 genome with Bowtie version 1.0.0 (*76*), allowing up to two mismatches and retaining uniquely mapped reads. Low-quality [mapping quality (MAPQ) <30], secondary, and unmapped reads were removed with samtools (*81*), and duplicates were marked using Picard MarkDuplicates version 1.127 (http://broadinstitute.github.io/picard/) (*82*). Strand-specific normalized coverage tracks were generated in R using the groHMM package (*83*), binned at 25 bp. UCSC-compatible wiggle files were converted to BigWig format using wigToBigWig for genome browser visualization (*84*). ChIP-seq peaks were identified using MACS version 1.4.2 (*85*) with default parameters. Signal enrichment around peak summits was visualized using deepTools (*85*, *86*). The computeMatrix tool was used in reference-point mode (--referencePoint center) to calculate normalized coverage ±5 kb around MACS peak summits. The resulting matrix was visualized using plotProfile.

ATAC-seq and analysis

Generation of ATAC-seq libraries and sequencing

ATAC-seq libraries were generated as previously described (*87*) with a few modifications. MCF-7 cells were grown and treated as described above, collected by trypsinization at the experimental end point, and counted. Fifty thousand live cells were used for each experimental condition. Nuclei were isolated by resuspending the cells in Hypotonic Lysis Buffer (10 mM tris, pH 7.6, 10 mM NaCl, 3 mM $MgCl_2$, 0.1% NP-40, 0.1% Tween 20, and 0.001% digitonin) and incubating on ice for 3 min. The nuclei were then washed once with Hypotonic Lysis Buffer without NP-40 or digitonin. The nuclei were then resuspended in Transposition Mix (10 mM tris, pH 7.6, 5 mM $MgCl_2$, 10% *N*,*N*′-dimethylformamide, 100 nM Tn5 transposase, 50 mM NaCl, 1 mM KCl, 5 mM Na_2HPO_4, 20% Tween 20, and 1% digitonin) and incubated at 37°C for 30 min with mixing at 1000 rpm. The resulting tagmented DNA fragments were purified by column purification using a Qiagen PCR purification kit (Qiagen, 28104). The final amplification of the libraries was performed using the NEBNext High-Fidelity Master Mix (NEB, M0541S) and Nextera i5 and i7 primers for a total of seven cycles. Excess adapters were removed from the libraries by using 1.3× volume of AMPure Purification beads (Beckman Coulter, A63881), and the libraries were sequenced on an Illumina NextSeq 2000 sequencer by paired-end sequencing.

Analysis of ATAC-seq data

The paired-end ATAC-seq reads were aligned to the human genome (hg38) using BWA-MEM version 0.7.15 (Li, 2013) with the -M flag to mark secondary alignments. Low-quality alignments (MAPQ <10) were removed using samtools (*81*), and alignments were sorted and deduplicated using Picard MarkDuplicates (REMOVE_DUPLICATES = true) (*82*, *88*). The final BAM files were indexed for downstream analyses (*82*, *89*). ATAC-seq peaks were identified using MACS2 version 2.1.0 (*85*) with paired-end BAM input (-f BAMPE). The resulting peaks were used for downstream accessibility and motif enrichment analyses (*90*). ATAC-seq signal tracks were generated in R using the WriteWiggleNorm function from the groHMM package (*83*) using bed files. Read coverage was binned in 25-bp windows and normalized to the average library size across all conditions. The resulting UCSC-style wiggle (.wig) files were converted to BigWig format using the UCSC wigToBigWig tool for visualization in genome browsers (*83*, *84*).

ATAC-seq peaks called by MACS2 were formatted into SAF (Simplified Annotation Format) using R and annotated with ChIPseeker (*91*). Genomic coordinates were converted into GRanges objects, and peaks were annotated relative to TSSs (±1 kb) using TxDb.Hsapiens.UCSC.hg38.knownGene and org.Hs.eg.db annotation databases. The distribution of peaks across genomic features (e.g., promoter, exon, intron, and intergenic) was visualized with pie charts

using plotAnnoPie (*92*, *93*). To examine chromatin accessibility at regions uniquely enriched in the ChIP-seq analyses, peak coordinates were extracted and used as reference points. Using the groHMM R package (*83*), read coverage from the ATAC-seq data was summarized across ±5-kb windows (100-bp bins) around these peak centers via the MetaGene function (*83*). Read counts were normalized by both the number of peaks and total reads per library, scaled to a common expected read depth. Resulting signal profiles were visualized using base R plotting functions.

PRO-seq and analysis

Nuclear run-on and RNA hydrolysis

Nuclear run-on and library preparation was performed following the PRO-seq protocol (*94*, *95*) using ~5 million MCF-7 nuclei per reaction with a few modifications. Nuclei in 50 μl of Storage Buffer were resuspended in 50 μl of 2× ROMM Buffer [10 mM tris-HCl, pH 8, 5 mM $MgCl_2$, 300 mM KCl, 40 μM each of Biotin-11-ATP/CTP/GTP/UTP (PerkinElmer, NEL544001EA, NEL542001EA, NEL545001EA, NEL543001EA), 1% Sarkosyl, 1 mM DTT, and 20 U of SUPERase-In RNase inhibitor] per reaction. Run-on reactions were incubated for 5 min at 37°C with gentle mixing. RNA was extracted by TRIzol LS (Invitrogen, 10296028), followed by ethanol precipitation. The resulting RNA was then sheared by base hydrolysis with 0.2 M NaOH for 10 min on ice and quenched with 500 mM tris-HCl, pH 6.8. Sheared RNA was subjected to salt exchange chromatography using Bio-Spin P30 columns (Bio-Rad, 7326250).

Enrichment of nascent RNA and preparation of PRO-seq libraries

Libraries were prepared using two biological replicates per condition. Sheared RNA was ligated to the VRA3 adaptor at the 3′ end using RNA ligase (NEB, M0204S) before enriching by binding to base-activated streptavidin C1 magnetic beads (Invitrogen, 65002). Enriched RNA was then subjected to on-bead 5′ hydroxyl repair using T4 polynucleotide kinase (NEB, M0201) in the presence of ATP (adenosine 5′-triphosphate), followed by 5′ decapping by RNA 5′ pyrophosphohydrolase (NEB, M0356S), and 5′ adaptor ligation to the VRA5 adaptor using RNA ligase. Ligated RNA was then eluted from the streptavidin beads by TRIzol (Invitrogen, 15596018), followed by ethanol precipitation. Single-stranded cDNA was generated by reverse transcription using Maxima H Minus RT enzyme (Thermo Fisher Scientific, EP0751). The resulting cDNA was then amplified using universal small RNA and indexed small RNA primers for a total of 13 cycles. Excess adaptors were removed using SPRI beads (Beckman Coulter, A63880). The quality of resulting libraries was assessed using the TapeStation 4150 Bioanalyzer system. Libraries were sequenced using an Illumina NextSeq 2000 by 100-bp single-end sequencing.

Analysis of PRO-seq data

The PRO-seq data quality was assessed using FastQC software (*1*). The data were then processed using a customized implementation of the proseq2.0 pipeline (*96*). The reads were aligned to the human genome (hg38) using the BWA aligner (*97*), excluding random chromosomes via a curated chromosome size file. The pipeline was executed in single-end, strand-specific mode (-SE -P -4DREG) for each sample. Strand-specific coverage was computed using deepTools bamCoverage version 2.3.5 with 50-bp binning and reads per kilobase of transcript per million mapped reads (RPKM) normalization (*86*, *96*). The resulting bedGraph files were converted to the BigWig format using bedGraphToBigWig (*84*), ensuring compatibility with the filtered hg38 chromosome sizes for accurate genome browser visualization.

HiC sequencing and analysis

Generation of HiC libraries

The Arima High Coverage HiC Kit (A410110) was used for all HiC experiments using the Standard Input Protocol as described by the manufacturer. Briefly, cells were treated with DMSO, 10 pM E2, or 10 nM E2 for 30 min as described above before harvesting. Each condition contained two independent biological replicates. The cells were then fixed using 2% formaldehyde, quenched using the Stop Solution provided with the kit, and counted using the Bio-Rad TC20 cell counter. Optimal starting material was estimated as described per the manufacturer's instruction, and 0.4×10^6 cells were used for each condition, which corresponded to 1.5 μg of DNA starting material. Digestion was performed using the Arima-HiC 2.0 RE Cocktail of four enzymes, followed by biotinylation of digested ends and proximity ligation according to the manufacturer's instructions. The fraction of proximally ligated DNA was quantified using the Arima-QC1 protocol, and samples were all confirmed to be >15% biotinylated.

Paired-end sequencing libraries were then prepared using the Arima Library Prep Module (Arima, A101030). Briefly, biotinylated and ligated DNA was sheared using a Covaris E220 Focused-ultrasonicator at 4°C, 105 peak incident power, 5% duty factor, and 200 cycles per burst for 70 s. Sizes were confirmed to be between 550 and 600 bp using an Agilent bioanalyzer. Two hundred nanograms of the resulting material was subjected to end repair, dA tailing, and adapter ligation, as described by the manufacturer. Libraries were amplified by PCR for 12 cycles and sequenced using a NovaSeq X Plus (PE150-25B) with the addition of 4% PhiX (Illumina, cat. no. 20151542). The libraries were sequenced to an approximate depth of 1 billion reads per condition.

Analysis of HiC data

Valid paired-end reads were generated using the HiC Pro pipeline (version 3.1.0) with the following modifications. A .bed file was generated for fragments generated by in silico digestion of the hg19 human genome using the digest_genome.py tool with restriction sites specific to the Arima High Coverage HiC kit. Unique molecular identifier sequences of the molecular barcode for each library were trimmed before any processing using this pipeline. A fragment size range cutoff of 10 to 100,000 was used. Alignment and filtering of singleton, MultiHits, low-MAPQ, and unmapped reads were done using the default settings. Iterative correction and eigenvector decomposition normalization was applied to valid pairs, and the resulting files were converted to .hic files using the hicpro2juicebox.py tool as part of the Juicer tool (*98*). TADs were identified using the Arrowhead feature of the JuiceBox toolkit (*98*) at a resolution of 10 kb, and loops were identified using the HiCCUPS function at multiple resolutions. Overlap between ChIP-seq data within TAD boundaries was determined using the intersect function, and distances between ChIP peaks within TADs were calculated using the closestBed function, both part of the bedtools kit. Contact maps were visualized using either the UCSC genome browser or HiCExplorer after Knight-Ruiz normalization.

Genomic data visualization

Heatmaps were created using Java Treeview (*99*) to visually display expression or enrichment that was significantly altered by the

experimental conditions. Biovenn (*100*) was used to construct Venn diagrams for up-regulated and down-regulated genes or peaks, with overlaps. Box plots were generated using custom R scripts to express FPKM (fragments per kilobase of transcript per million mapped reads) values across the experimental conditions. Statistical significance among these comparisons was determined using Wilcoxon rank-sum tests ($P < 0.05$).

Rapid immunoprecipitation MS of endogenous proteins (RIME)

Immunoprecipitation

Rapid immunoprecipitation followed by MS analysis was performed using MCF-7 cells as previously described (*101*) with a few modifications. Each condition had a minimum of four independent biological replicates. Approximately 10^8 cells were used per experimental condition. Briefly, magnetic protein A Dynabeads were first blocked in bovine serum albumin (5 mg/ml) in 1× PBS for 30 min at room temperature. A polyclonal ERα antibody was added to the blocked beads overnight at 4°C with gentle mixing. The beads were then washed twice and resuspended in radioimmunoprecipitation assay buffer [50 mM Hepes, pH 7.6, 1 mM EDTA, 0.7% (w/v) sodium deoxycholate, 1% (v/v) NP-40, 500 mM LiCl, and 1× protease inhibitor cocktail] until further use.

At the end of the experiments, the cells were cross-linked using 1% formaldehyde for 10 min at room temperature and quenched by adding glycine to a final concentration of 100 mM. The cells were washed twice in ice-cold 1× PBS and then collected by scraping in 1× PBS. The cells were incubated in Lysis Buffer 1 [50 mM Hepes, pH 7.5, 140 mM NaCl, 1 mM EDTA, 10% (v/v) glycerol, 0.5% (v/v) IGEPAL CA-630, 0.25% (v/v) Triton X-100, and 1× protease inhibitor cocktail] for 10 min on ice. The resulting nuclei were pelleted and washed with Lysis Buffer 2 (10 mM tris, pH 8.0, 200 mM NaCl, 1 mM EDTA, 0.5 mM EGTA, and 1× protease inhibitor cocktail) and pelleted. The nuclei were then lysed using Lysis Buffer 3 [10 mM tris, pH 8.0, 100 mM NaCl, 1 mM EDTA, 0.5 mM EGTA, 0.1% (w/v) sodium deoxycholate, 0.5% (v/v) *N*-lauroylsarcosine, and 1× protease inhibitor cocktail] and sonicated for 10 min (30 s on/30 s off) using the Diagenode Pico sonicator. The sheared chromatin was cleared of debris by applying Triton X-100 to a final concentration of 1% (v/v), followed by centrifugation at >20,000*g* for 10 min at 4°C. The clarified chromatin samples were then applied to the antibody-loaded beads overnight at 4°C with gentle mixing. The chromatin-immune complexes on the beads were washed seven times with radioimmunoprecipitation assay buffer, followed by two washes in 100 mM ammonium hydrogen carbonate solution to remove the detergents. Beads were resuspended in ammonium hydrogen carbonate and decross-linked by boiling at 95°C for 10 min.

Mass spectrometry

After reduction and alkylation with tris(2-carboxyethyl) phosphine hydrochloride (Sigma-Aldrich, 646547-10X1ML) and iodoacetamide (Sigma-Aldrich, I1149-5G), the samples were digested overnight with trypsin (Pierce, 90057). After solid-phase extraction cleanup with an Oasis HLB μelution plate (Waters), the resulting peptides were reconstituted in 2% (v/v) acetonitrile (ACN) and 0.1% trifluoroacetic acid in water to a concentration of about 0.5 μg/μl. Two microliters of each sample was injected onto a Q Exactive HF mass spectrometer coupled to an Ultimate 3000 RSLC-Nano liquid chromatography system with a 75-μm-inner-diameter, 15-cm-long EasySpray column (Thermo Fisher Scientific, ES75150PN) and eluted with a gradient from 0 to 28% buffer B over 90 min. Buffer A contained 2% (v/v) ACN and 0.1% formic acid in water, and buffer B contained 80% (v/v) ACN, 10% (v/v) trifluoroethanol, and 0.1% formic acid in water. The mass spectrometer operated in positive ion mode with a source voltage of 2.5 kV and an ion transfer tube temperature of 300°C. MS scans were acquired at 120,000 resolution in the Orbitrap, and up to 20 tandem MS spectra were obtained in the ion trap for each full spectrum acquired using higher-energy collisional dissociation for ions with charges 2 to 8. Dynamic exclusion was set for 20 s after an ion was selected for fragmentation.

MS data analyses

Raw MS data files were analyzed using Proteome Discoverer version 3.0 (Thermo Fisher Scientific; RRID: SCR_014477), with peptide identification performed using Sequest HT searching against the human-reviewed protein database from UniProt. Fragment and precursor tolerances of 10 parts per million and 0.02 Da were specified, and three missed cleavages were allowed. Carbamidomethylation of Cys was set as a fixed modification, and oxidation of Met was set as a variable modification. The false discovery rate cutoff was 1% for all peptides. Peptide peak intensities were summed for all peptides matched to a protein for protein quantitation.

Significance of enrichment differences between the E2 treatment and vehicle control values was calculated for each identified protein using Student's *t* test. Proteins with $P < 0.05$ were used for further analysis. Relative abundances were calculated by dividing the abundance values found from the ERα immunoprecipitations with the corresponding IgG control precipitations. The E2 dose at the which relative abundance was maximal was calculated using the max() function in R, and each identified protein was categorized as such. The DAVID (Database for Annotation, Visualization, and Integrated Discovery) online tool (*102*) was used to determine enriched GO terms for these categories (see below).

GO and gene set enrichment analyses

GO analysis

GO analysis of the RNA-seq data was conducted using the DAVID online tool (*102*), and the ontological terms were ranked on the basis of enrichment scores.

KEGG analysis

Gene set enrichment analysis was performed on RNA-seq differential expression data using KEGG analysis (*103*) with the clusterProfiler R package using a *P* cutoff of <0.05.

DNA sequence motif analyses

HOMER analysis

De novo motif analysis was performed using the HOMER findmotifGenome.pl command line (*104*), and known motifs were used for subsequent analyses. For motif analysis around ChIP-seq peaks, these analyses were performed on a 200-bp region surrounding the peak summits. For analyses performed on open chromatin regions, ATAC-seq data were used, and the analyses were done within the peak range (-d given). Gene logos were obtained from the corresponding motifs using the JASPAR database (*105*).

Find individual motif occurrences (FIMO) analysis

Find individual motif occurrences (FIMO) (*106*) analysis was performed to identify motifs within initially opened and newly opened regions of individual gene regions. Regions of interest were identified on the basis of peak occurrences in ATAC-seq data. DNA sequences within these regions were uploaded as a .fasta file to the

FIMO web tool in the MEME Suite 5.5.8 (*107*) using a *P* cutoff of <0.005.

Modeling the fractional occupancy of ERα on DNA

To quantify the fractional occupancy (θ) of ERα on DNA across a range of hormone and receptor concentrations, we used computational modeling on the basis of assumptions, parameters, and understanding of steroid hormone receptor activity strongly supported in the literature. The analysis was developed on the basis of models, analyses, and data from the literature as specified below and stimulated using R. The results from this analysis are shown in Fig. 3 (E and F) and table S3.

Model overview and mathematical framework

We used a steady-state equilibrium model for our analyses. This model accounts for a multistep assembly of the active receptor complex. The fractional occupancy is defined by the following equilibrium expression with the terms as specified below the equation

$$\theta = \frac{[E2]^2}{[E2]^2 + \left(\frac{K_2 K_3}{[ER]^2}\right)\left([E2] + K_1\right)^2}$$

where [E2] is the estradiol concentration (nM), [ER] is the ERα concentration (μM), K_1 is the K_d for E2 binding to ERα, K_2 is the K_d for dimerization ERα, and K_3 is the K_d for ERα dimer binding to ERE DNA.

Thermodynamic parameters

The model incorporates three distinct equilibrium K_d's to define the energetic barriers of receptor activation, with estimated values derived from a range of empirical determinations found in the literature: (i) ligand binding (K_1): representing the high-affinity binding of E2 to the ERα monomer, set to 0.1 nM (*108*–*118*); (ii) dimerization (K_2): governing the assembly of two E2-ERα complexes, set to 2.5 nM (*119*–*121*); (iii) DNA association (K_3): describing the affinity of the finalized homodimer for the ERE, set to 0.5 nM (*115*, *122*, *123*).

Mechanistic assumptions

The analysis is predicated on the following biological and physical assumptions derived from the literature and stoichiometric requirements: (i) System equilibrium: The association and dissociation rates of all components are assumed to be in steady-state equilibrium; (ii) ERα homodimer activity: The model assumes that the active, DNA binding–capable form of the receptor is a homodimer (ERα-ERα); (iii) cooperativity: A Hill coefficient of approximately $n = 2$ is assumed, reflecting a requirement for two molecules of E2 to facilitate the formation of a single functional ERα dimer; (iv) receptor conservation: The initial concentration of the receptor ($ERα_{Initial}$) is considered to be approximately equal to the total receptor concentration ($ERα_{Total}$), assuming that the fraction of receptor sequestered by DNA does not significantly deplete the total nuclear pool.

Estimation of parameter values

We collected values for all of the parameters used in the formula above from a minimum of two sources in the literature but typically more (see citations throughout this section). In all cases, the sources collectively provided a range of values for which we standardized the units, evaluated the quality and reliability of the assays used, and selected a value within the range provided. Value selections were made on the basis of the frequency with which the value (or a similar value) was reported, as well as the quality of the assay and the data. We estimated the ERα concentrations in MCF-7 cells (*124*–*135*), T-47D cells (*112*, *130*, *133*, *134*, *136*, *137*) MDA-MB-361 cells (*130*, *134*) and rodent myometrial cells (*138*–*142*) on the basis of the literature, with adjustments made on the basis of our quantitative Western blotting (Fig. 3A). Values reported as femtomoles of ERα/milligram of DNA or femtomoles of ERα/milligram of protein were converted to micromolar using common assumptions about cell size, DNA concentrations, and protein concentrations derived from the literature. The values used in our calculations were as follows: MCF-7 cells, 0.1 μM; T-47D cells, 0.04 μM; MDA-MB-361 cells, 0.01 μM; rodent myometrial cells, 0.02 μM.

Survival plots

Kaplan-Meier curves for overall survival analyses were made using the GEPIA2 open-source database containing RNA-seq gene expression data (*143*). The data were first sorted for all patients with breast cancer, followed by the luminal A molecular subtype and lastly by gene signature. A quartile cutoff was applied, and patients falling under a 95% confidence interval was plotted over a 5-year period.

Statistical analyses

All genomic analyses were performed at a minimum of two individual biological replicates. Statistical analysis for the genomic experiments was performed using standard genomic statistical tests. All qPCR-based experiments had a minimum of three independent biological replicates. All statistical tests used and their corresponding *P* values are provided in the figure legends. Student's *t* tests were used for pairwise comparisons, a one-way analysis of variance (ANOVA) was used for group comparisons, and Tukey's post hoc test was applied to correct for multiple comparisons as needed. Comparisons between fold changes within sequencing data used a *q* cutoff of <0.01; the *q* values correct for multiple comparisons and are adjusted for false discovery rates. Last, Wilcoxon rank-sum tests were used to compare distributions between conditions as needed.

Supplementary Materials

This PDF file includes:

Figs. S1 to S9
Tables S1 to S3

REFERENCES

1. H. Kronenberg, S. Melmed, K. Polonsky, P. R. Larsen, Eds., *Williams Textbook of Endocrinology* (Saunders Elsevier, 2007).
2. S. C. Hewitt, J. C. Harrell, K. S. Korach, Lessons in estrogen biology from knockout and transgenic animals. *Annu. Rev. Physiol.* **67**, 285–308 (2005).
3. P. Chen, B. Li, L. Ou-Yang, Role of estrogen receptors in health and disease. *Front. Endocrinol. (Lausanne)* **13**, 839005 (2022).
4. F. Pakdel, The role of estrogen receptors in health and disease. *Int. J. Mol. Sci.* **24**, 11354 (2023).
5. K. J. Hamilton, S. C. Hewitt, Y. Arao, K. S. Korach, Estrogen hormone biology. *Curr. Top. Dev. Biol.* **125**, 109–146 (2017).
6. K. A. Burns, K. S. Korach, Estrogen receptors and human disease: An update. *Arch. Toxicol.* **86**, 1491–1504 (2012).
7. J. V. V. Isola, S. Ko, S. R. Ocanas, M. B. Stout, Role of estrogen receptor alpha in aging and chronic disease. *Adv. Geriatr. Med. Res.* **5**, e230005 (2023).
8. J. M. Matyi, G. B. Rattinger, S. Schwartz, M. Buhusi, J. T. Tschanz, Lifetime estrogen exposure and cognition in late life: The cache county study. *Menopause* **26**, 1366–1374 (2019).
9. G. Pesce, F. Artaud, E. Roze, I. Degaey, B. Portugal, T. T. H. Nguyen, A. Fournier, M. C. Boutron-Ruault, G. Severi, A. Elbaz, M. Canonico, Reproductive characteristics, use of exogenous hormones and Parkinson disease in women from the E3N study. *Brain* **146**, 2535–2546 (2023).
10. S. Jett, N. Malviya, E. Schelbaum, G. Jang, E. Jahan, K. Clancy, H. Hristov, S. Pahlajani, K. Niotis, S. Loeb-Zeitlin, Y. Havryliuk, R. Isaacson, R. D. Brinton, L. Mosconi, Endogenous and exogenous estrogen exposures: How women's reproductive health can drive brain aging and inform Alzheimer's prevention. *Front. Aging Neurosci.* **14**, 831807 (2022).
11. E. Carmina, F. Z. Stanczyk, R. A. Lobo, "Laboratory assessment" in *Yen & Jaffe's Reproductive Endocrinology: Physiology, Pathophysiology, and Clinical Management*, J. F. Strauss, R. L. Barbieri, Eds. (Elsevier-Saunders, ed. 7, 2013), chap. 34.

12. J. P. Holst, O. P. Soldin, T. Guo, S. J. Soldin, Steroid hormones: Relevance and measurement in the clinical laboratory. *Clin. Lab. Med.* **24**, 105–118 (2004).
13. J. F. Couse, K. S. Korach, Estrogen receptor null mice: What have we learned and where will they lead us? *Endocr. Rev.* **20**, 358–417 (1999).
14. M. Warner, S. Nilsson, J. A. Gustafsson, The estrogen receptor family. *Curr. Opin. Obstet. Gynecol.* **11**, 249–254 (1999).
15. W. J. Welboren, F. C. Sweep, P. N. Span, H. G. Stunnenberg, Genomic actions of estrogen receptor alpha: What are the targets and how are they regulated? *Endocr. Relat. Cancer* **16**, 1073–1089 (2009).
16. A. Hecht, A. Berkenstam, P. E. Stromstedt, J. A. Gustafsson, A. E. Sippel, A progesterone responsive element maps to the far upstream steroid dependent DNase hypersensitive site of chicken lysozyme chromatin. *EMBO J.* **7**, 2063–2073 (1988).
17. H. M. Jantzen, U. Strahle, B. Gloss, F. Stewart, W. Schmid, M. Boshart, R. Miksicek, G. Schutz, Cooperativity of glucocorticoid response elements located far upstream of the tyrosine aminotransferase gene. *Cell* **49**, 29–38 (1987).
18. J. K. Nyborg, S. R. Spindler, Alterations in local chromatin structure accompany thyroid hormone induction of growth hormone gene transcription. *J. Biol. Chem.* **261**, 5685–5688 (1986).
19. S. J. Usala, W. S. Young III, H. Morioka, V. M. Nikodem, The effect of thyroid hormone on the chromatin structure and expression of the malic enzyme gene in hepatocytes. *Mol. Endocrinol.* **2**, 619–626 (1988).
20. K. S. Zaret, K. R. Yamamoto, Reversible and persistent changes in chromatin structure accompany activation of a glucocorticoid-dependent enhancer element. *Cell* **38**, 29–38 (1984).
21. M. L. Acevedo, W. L. Kraus, Transcriptional activation by nuclear receptors. *Essays Biochem.* **40**, 73–88 (2004).
22. S. C. Biddie, S. John, G. L. Hager, Genome-wide mechanisms of nuclear receptor action. *Trends Endocrinol. Metab.* **21**, 3–9 (2010).
23. C. K. Glass, M. G. Rosenfeld, The coregulator exchange in transcriptional functions of nuclear receptors. *Genes Dev.* **14**, 121–141 (2000).
24. D. M. Lonard, B. W. O'Malley, Nuclear receptor coregulators: Modulators of pathology and therapeutic targets. *Nat. Rev. Endocrinol.* **8**, 598–604 (2012).
25. N. J. McKenna, R. B. Lanz, B. W. O'Malley, Nuclear receptor coregulators: Cellular and molecular biology. *Endocr. Rev.* **20**, 321–344 (1999).
26. E. Cheung, W. L. Kraus, Genomic analyses of hormone signaling and gene regulation. *Annu. Rev. Physiol.* **72**, 191–218 (2010).
27. J. H. Martens, N. A. Rao, H. G. Stunnenberg, Genome-wide interplay of nuclear receptors with the epigenome. *Biochim. Biophys. Acta* **1812**, 818–823 (2011).
28. N. Hah, C. G. Danko, L. Core, J. J. Waterfall, A. Siepel, J. T. Lis, W. L. Kraus, A rapid, extensive, and transient transcriptional response to estrogen signaling in breast cancer cells. *Cell* **145**, 622–634 (2011).
29. N. Hah, S. Murakami, A. Nagari, C. G. Danko, W. L. Kraus, Enhancer transcripts mark active estrogen receptor binding sites. *Genome Res.* **23**, 1210–1223 (2013).
30. J. S. Carroll, X. S. Liu, A. S. Brodsky, W. Li, C. A. Meyer, A. J. Szary, J. Eeckhoute, W. Shao, E. V. Hestermann, T. R. Geistlinger, E. A. Fox, P. A. Silver, M. Brown, Chromosome-wide mapping of estrogen receptor binding reveals long-range regulation requiring the forkhead protein FoxA1. *Cell* **122**, 33–43 (2005).
31. J. S. Carroll, C. A. Meyer, J. Song, W. Li, T. R. Geistlinger, J. Eeckhoute, A. S. Brodsky, E. K. Keeton, K. C. Fertuck, G. F. Hall, Q. Wang, S. Bekiranov, V. Sementchenko, E. A. Fox, P. A. Silver, T. R. Gingeras, X. S. Liu, M. Brown, Genome-wide analysis of estrogen receptor binding sites. *Nat. Genet.* **38**, 1289–1297 (2006).
32. C. Y. Lin, V. B. Vega, J. S. Thomsen, T. Zhang, S. L. Kong, M. Xie, K. P. Chiu, L. Lipovich, D. H. Barnett, F. Stossi, A. Yeo, J. George, V. A. Kuznetsov, Y. K. Lee, T. H. Charn, N. Palanisamy, L. D. Miller, E. Cheung, B. S. Katzenellenbogen, Y. Ruan, G. Bourque, C. L. Wei, E. T. Liu, Whole-genome cartography of estrogen receptor alpha binding sites. *PLOS Genet.* **3**, e87 (2007).
33. S. C. Hewitt, L. Li, S. A. Grimm, Y. Chen, L. Liu, Y. Li, P. R. Bushel, D. Fargo, K. S. Korach, Research resource: Whole-genome estrogen receptor alpha binding in mouse uterine tissue revealed by ChIP-seq. *Mol. Endocrinol.* **26**, 887–898 (2012).
34. S. K. Tan, Z. H. Lin, C. W. Chang, V. Varang, K. R. Chng, Y. F. Pan, E. L. Yong, W. K. Sung, E. Cheung, AP-2γ regulates oestrogen receptor-mediated long-range chromatin interaction and gene transcription. *EMBO J.* **30**, 2569–2581 (2011).
35. A. Hurtado, K. A. Holmes, C. S. Ross-Innes, D. Schmidt, J. S. Carroll, FOXA1 is a key determinant of estrogen receptor function and endocrine response. *Nat. Genet.* **43**, 27–33 (2011).
36. C. E. Foulds, Q. Feng, C. Ding, S. Bailey, T. L. Hunsaker, A. Malovannaya, R. A. Hamilton, L. A. Gates, Z. Zhang, C. Li, D. Chan, A. Bajaj, C. G. Callaway, D. P. Edwards, D. M. Lonard, S. Y. Tsai, M. J. Tsai, J. Qin, B. W. O'Malley, Proteomic analysis of coregulators bound to ERα on DNA and nucleosomes reveals coregulator dynamics. *Mol. Cell* **51**, 185–199 (2013).
37. M. J. Fullwood, M. H. Liu, Y. F. Pan, J. Liu, H. Xu, Y. B. Mohamed, Y. L. Orlov, S. Velkov, A. Ho, P. H. Mei, E. G. Chew, P. Y. Huang, W. J. Welboren, Y. Han, H. S. Ooi, P. N. Ariyaratne, V. B. Vega, Y. Luo, P. Y. Tan, P. Y. Choy, K. D. Wansa, B. Zhao, K. S. Lim, S. C. Leow, J. S. Yow, R. Joseph, H. Li, K. V. Desai, J. S. Thomsen, Y. K. Lee, R. K. Karuturi, T. Herve, G. Bourque, H. G. Stunnenberg, X. Ruan, V. Cacheux-Rataboul, W. K. Sung, E. T. Liu, C. L. Wei, E. Cheung, Y. Ruan, An oestrogen-receptor-α-bound human chromatin interactome. *Nature* **462**, 58–64 (2009).
38. D. Shlyueva, G. Stampfel, A. Stark, Transcriptional enhancers: From properties to genome-wide predictions. *Nat. Rev. Genet.* **15**, 272–286 (2014).
39. H. H. He, C. A. Meyer, M. W. Chen, V. C. Jordan, M. Brown, X. S. Liu, Differential DNase I hypersensitivity reveals factor-dependent chromatin dynamics. *Genome Res.* **22**, 1015–1025 (2012).
40. M. F. Melgar, F. S. Collins, P. Sethupathy, Discovery of active enhancers through bidirectional expression of short transcripts. *Genome Biol.* **12**, R113 (2011).
41. G. Natoli, J. C. Andrau, Noncoding transcription at enhancers: General principles and functional models. *Annu. Rev. Genet.* **46**, 1–19 (2012).
42. M. Bulger, M. Groudine, Functional and mechanistic diversity of distal transcription enhancers. *Cell* **144**, 327–339 (2011).
43. N. Hah, W. L. Kraus, Hormone-regulated transcriptomes: Lessons learned from estrogen signaling pathways in breast cancer cells. *Mol. Cell. Endocrinol.* **382**, 652–664 (2014).
44. T. Y. Hou, W. L. Kraus, Spirits in the material world: Enhancer RNAs in transcriptional regulation. *Trends Biochem. Sci.* **46**, 138–153 (2021).
45. S. C. Hewitt, S. A. Grimm, S. P. Wu, F. J. DeMayo, K. S. Korach, Estrogen receptor alpha (ERα)-binding super-enhancers drive key mediators that control uterine estrogen responses in mice. *J. Biol. Chem.* **295**, 8387–8400 (2020).
46. D. Bojcsuk, G. Nagy, B. L. Balint, Alternatively constructed estrogen receptor α-driven super-enhancers result in similar gene expression in breast and endometrial cell lines. *Int. J. Mol. Sci.* **21**, 1630 (2020).
47. F. Le Dily, M. Beato, TADs as modular and dynamic units for gene regulation by hormones. *FEBS Lett.* **589**, 2885–2892 (2015).
48. J. Achinger-Kawecka, F. Valdes-Mora, P. L. Luu, K. A. Giles, C. E. Caldon, W. Qu, S. Nair, S. Soto, W. J. Locke, N. S. Yeo-Teh, C. M. Gould, Q. Du, G. C. Smith, I. R. Ramos, K. F. Fernandez, D. S. Hoon, J. M. W. Gee, C. Stirzaker, S. J. Clark, Epigenetic reprogramming at estrogen-receptor binding sites alters 3D chromatin landscape in endocrine-resistant breast cancer. *Nat. Commun.* **11**, 320 (2020).
49. A. R. Barutcu, B. R. Lajoie, R. P. McCord, C. E. Tye, D. Hong, T. L. Messier, G. Browne, A. J. van Wijnen, J. B. Lian, J. L. Stein, J. Dekker, A. N. Imbalzano, G. S. Stein, Chromatin interaction analysis reveals changes in small chromosome and telomere clustering between epithelial and breast cancer cells. *Genome Biol.* **16**, 214 (2015).
50. T. Paszkowski, M. Binkowska, R. Debski, M. Krzyczkowska-Sendrakowska, V. Skrzypulec-Plinta, W. Zgliczynski, Menopausal hormone therapy in questions and answers—A manual for physicians of various specialties. *Prz Menopauzalny* **18**, 1–8 (2019).
51. R. Ansbacher, Low-dose oral contraceptives: Health consequences of discontinuation. *Contraception* **62**, 285–288 (2000).
52. L. Cho, A. M. Kaunitz, S. S. Faubion, S. N. Hayes, E. S. Lau, N. Pristera, N. Scott, J. L. Shifren, C. L. Shufelt, C. A. Stuenkel, K. J. Lindley, ACC CVD in Women Committee, Rethinking menopausal hormone therapy: For whom, what, when, and how long? *Circulation* **147**, 597–610 (2023).
53. Z. Li, F. Chen, L. Chen, J. Liu, D. Tseng, F. Hadi, S. Omarjee, K. Kishore, J. Kent, J. Kirkpatrick, C. D'Santos, M. Lawson, J. Gertz, M. J. Sikora, D. P. McDonnell, J. S. Carroll, K. Polyak, S. Oesterreich, A. V. Lee, EstroGene2.0: A multi-omic database of response to estrogens, ER-modulators, and resistance to endocrine therapies in breast cancer. bioRxiv 601163 (2024); www.biorxiv.org/content/10.1101/2024.06.28.601163v1.
54. E. M. Martin, K. A. Orlando, K. Yokobori, P. A. Wade, The estrogen receptor/GATA3/FOXA1 transcriptional network: Lessons learned from breast cancer. *Curr. Opin. Struct. Biol.* **71**, 65–70 (2021).
55. M. Takaku, S. A. Grimm, B. De Kumar, B. D. Bennett, P. A. Wade, Cancer-specific mutation of GATA3 disrupts the transcriptional regulatory network governed by Estrogen Receptor alpha, FOXA1 and GATA3. *Nucleic Acids Res.* **48**, 4756–4768 (2020).
56. V. Theodorou, R. Stark, S. Menon, J. S. Carroll, GATA3 acts upstream of FOXA1 in mediating ESR1 binding by shaping enhancer accessibility. *Genome Res.* **23**, 12–22 (2013).
57. H. Mohammed, C. Taylor, G. D. Brown, E. K. Papachristou, J. S. Carroll, C. S. D'Santos, Rapid immunoprecipitation mass spectrometry of endogenous proteins (RIME) for analysis of chromatin complexes. *Nat. Protoc.* **11**, 316–326 (2016).
58. H. Gao, S. Falt, A. Sandelin, J. A. Gustafsson, K. Dahlman-Wright, Genome-wide identification of estrogen receptor α-binding sites in mouse liver. *Mol. Endocrinol.* **22**, 10–22 (2008).
59. P. J. Kushner, D. A. Agard, G. L. Greene, T. S. Scanlan, A. K. Shiau, R. M. Uht, P. Webb, Estrogen receptor pathways to AP-1. *J. Steroid Biochem. Mol. Biol.* **74**, 311–317 (2000).
60. L. Core, K. Adelman, Promoter-proximal pausing of RNA polymerase II: A nexus of gene regulation. *Genes Dev.* **33**, 960–982 (2019).
61. T. Y. Hou, W. L. Kraus, Analysis of estrogen-regulated enhancer RNAs identifies a functional motif required for enhancer assembly and gene expression. *Cell Rep.* **39**, 110944 (2022).

62. M. P. Jansen, T. Knijnenburg, E. A. Reijm, I. Simon, R. Kerkhoven, M. Droog, A. Velds, S. van Laere, L. Dirix, X. Alexi, J. A. Foekens, L. Wessels, S. C. Linn, E. M. Berns, W. Zwart, Hallmarks of aromatase inhibitor drug resistance revealed by epigenetic profiling in breast cancer. *Cancer Res.* **73**, 6632–6641 (2013).
63. A. L. Han, K. Vinod Paul, S. Rao, H. M. Brechbuhl, C. A. Sartorius, S. Ramachandran, P. Kabos, Estradiol (E2) concentration shapes the chromatin binding landscape of estrogen receptor alpha. *J. Biol. Chem.* **301**, 108499 (2025).
64. J. Trendel, S. Trendel, S. Sha, F. Greulich, S. Goll, S. I. Wudy, K. Kleigrewe, S. Kubicek, N. H. Uhlenhaut, B. Kuster, The human proteome with direct physical access to DNA. *Cell* **188**, 4424–4440.e17 (2025).
65. R. Safi, S. E. Wardell, P. Watkinson, X. Qin, M. Lee, S. Park, T. Krebs, E. L. Dolan, A. Blattler, T. Tsuji, S. Nayak, M. Khater, C. Fontanillo, M. A. Newlin, M. L. Kirkland, Y. Xie, H. Long, E. C. Fink, S. W. Fanning, S. Runyon, M. Brown, S. Xu, K. Owzar, J. D. Norris, D. P. McDonnell, Androgen receptor monomers and dimers regulate opposing biological processes in prostate cancer cells. *Nat. Commun.* **15**, 7675 (2024).
66. P. Polak, E. Domany, Alu elements contain many binding sites for transcription factors and may play a role in regulation of developmental processes. *BMC Genomics* **7**, 133 (2006).
67. M. Su, D. Han, J. Boyd-Kirkup, X. Yu, J. J. Han, Evolution of Alu elements toward enhancers. *Cell Rep.* **7**, 376–385 (2014).
68. J. Norris, D. Fan, C. Aleman, J. R. Marks, P. A. Futreal, R. W. Wiseman, J. D. Iglehart, P. L. Deininger, D. P. McDonnell, Identification of a new subclass of Alu DNA repeats which can function as estrogen receptor-dependent transcriptional enhancers. *J. Biol. Chem.* **270**, 22777–22782 (1995).
69. S. Naqvi, S. Kim, H. Hoskens, H. S. Matthews, R. A. Spritz, O. D. Klein, B. Hallgrimsson, T. Swigut, P. Claes, J. K. Pritchard, J. Wysocka, Precise modulation of transcription factor levels identifies features underlying dosage sensitivity. *Nat. Genet.* **55**, 841–851 (2023).
70. Y. Kamei, L. Xu, T. Heinzel, J. Torchia, R. Kurokawa, B. Gloss, S. C. Lin, R. A. Heyman, D. W. Rose, C. K. Glass, M. G. Rosenfeld, A CBP integrator complex mediates transcriptional activation and AP-1 inhibition by nuclear receptors. *Cell* **85**, 403–414 (1996).
71. W. L. Kraus, J. T. Kadonaga, p300 and estrogen receptor cooperatively activate transcription via differential enhancement of initiation and reinitiation. *Genes Dev.* **12**, 331–342 (1998).
72. H. B. Kim, W. L. Kraus, Intracellular retention of estradiol Is mediated by GRAM domain-containing protein ASTER-B in breast cancer cells. *Mol. Cancer Res.* **23**, 313–326 (2025).
73. S. Andrews, "FastQC. A quality control tool for high throughput sequence data" (2010); www.bioinformatics.babraham.ac.uk/projects/fastqc.
74. ENCODE Project Consortium, M. P. Snyder, T. R. Gingeras, J. E. Moore, Z. Weng, M. B. Gerstein, B. Ren, R. C. Hardison, J. A. Stamatoyannopoulos, B. R. Graveley, E. A. Feingold, M. J. Pazin, M. Pagan, D. A. Gilchrist, B. C. Hitz, J. M. Cherry, B. E. Bernstein, E. M. Mendenhall, D. R. Zerbino, A. Frankish, P. Flicek, R. M. Myers, Perspectives on ENCODE. *Nature* **583**, 693–698 (2020).
75. D. Kim, G. Pertea, C. Trapnell, H. Pimentel, R. Kelley, S. L. Salzberg, TopHat2: Accurate alignment of transcriptomes in the presence of insertions, deletions and gene fusions. *Genome Biol.* **14**, R36 (2013).
76. B. Langmead, C. Trapnell, M. Pop, S. L. Salzberg, Ultrafast and memory-efficient alignment of short DNA sequences to the human genome. *Genome Biol.* **10**, R25 (2009).
77. C. Trapnell, L. Pachter, S. L. Salzberg, TopHat: Discovering splice junctions with RNA-Seq. *Bioinformatics* **25**, 1105–1111 (2009).
78. Y. Liao, G. K. Smyth, W. Shi, featureCounts: An efficient general purpose program for assigning sequence reads to genomic features. *Bioinformatics* **30**, 923–930 (2014).
79. M. I. Love, W. Huber, S. Anders, Moderated estimation of fold change and dispersion for RNA-seq data with DESeq2. *Genome Biol.* **15**, 550 (2014).
80. M. Martin, Cutadapt removes adapter sequences from high-throughput sequencing reads. *EMBnet.journal* **17**, 10–12 (2011).
81. H. Li, B. Handsaker, A. Wysoker, T. Fennell, J. Ruan, N. Homer, G. Marth, G. Abecasis, R. Durbin, 1000 Genome Project Data Processing Subgroup, The sequence alignment/map format and SAMtools. *Bioinformatics* **25**, 2078–2079 (2009).
82. Broad Institute, "Picard toolkit," GitHub Repository (2017); https://github.com/broadinstitute/picard.
83. M. Chae, C. G. Danko, W. L. Kraus, groHMM: A computational tool for identifying unannotated and cell type-specific transcription units from global run-on sequencing data. *BMC Bioinformatics* **16**, 222 (2015).
84. W. J. Kent, A. S. Zweig, G. Barber, A. S. Hinrichs, D. Karolchik, BigWig and BigBed: Enabling browsing of large distributed datasets. *Bioinformatics* **26**, 2204–2207 (2010).
85. Y. Zhang, T. Liu, C. A. Meyer, J. Eeckhoute, D. S. Johnson, B. E. Bernstein, C. Nusbaum, R. M. Myers, M. Brown, W. Li, X. S. Liu, Model-based analysis of ChIP-Seq (MACS). *Genome Biol.* **9**, R137 (2008).
86. F. Ramirez, D. P. Ryan, B. Gruning, V. Bhardwaj, F. Kilpert, A. S. Richter, S. Heyne, F. Dundar, T. Manke, deepTools2: A next generation web server for deep-sequencing data analysis. *Nucleic Acids Res.* **44**, W160–W165 (2016).
87. D. Huang, C. V. Camacho, S. Martire, A. Nagari, R. Setlem, X. Gong, A. D. Edwards, S. P. Chiu, L. A. Banaszynski, W. L. Kraus, Oncohistone mutations occur at functional sites of regulatory ADP-ribosylation. *Cancer Res.* **82**, 2361–2377 (2022).
88. H. Li, R. Durbin, Fast and accurate short read alignment with Burrows-Wheeler transform. *Bioinformatics* **25**, 1754–1760 (2009).
89. H. Li, Aligning sequence reads, clone sequences and assembly contigs with BWA-MEM. arXiv:1303.3997 (2013); https://arxiv.org/abs/1303.3997.
90. J. Feng, T. Liu, B. Qin, Y. Zhang, X. S. Liu, Identifying ChIP-seq enrichment using MACS. *Nat. Protoc.* **7**, 1728–1740 (2012).
91. G. Yu, L. G. Wang, Q. Y. He, ChIPseeker: An R/Bioconductor package for ChIP peak annotation, comparison and visualization. *Bioinformatics* **31**, 2382–2383 (2015).
92. M. Carlson, "TxDb.Hsapiens.UCSC.hg38.knownGene: Annotation package for TxDb object(s)," R package version 3.18.0 (2023).
93. M. Carlson, "org.Hs.eg.db: Genome wide annotation for Human," R package version 3.18.0 (2023).
94. J. Judd, L. A. Wojenski, L. M. Wainman, N. D. Tippens, E. J. Rice, A. Dziubek, G. J. Villafano, E. M. Wissink, P. Versluis, L. Bagepalli, S. R. Shah, D. B. Mahat, J. M. Tome, C. G. Danko, J. T. Lis, L. J. Core, A rapid, sensitive, scalable method for Precision Run-On sequencing (PRO-seq). bioRxiv 102277 (2020); www.biorxiv.org/content/10.1101/2020.05.18.102277v1.
95. D. B. Mahat, H. Kwak, G. T. Booth, I. H. Jonkers, C. G. Danko, R. K. Patel, C. T. Waters, K. Munson, L. J. Core, J. T. Lis, Base-pair-resolution genome-wide mapping of active RNA polymerases using precision nuclear run-on (PRO-seq). *Nat. Protoc.* **11**, 1455–1476 (2016).
96. C. G. Danko, S. L. Hyland, L. J. Core, A. L. Martins, C. T. Waters, H. W. Lee, V. G. Cheung, W. L. Kraus, J. T. Lis, A. Siepel, Identification of active transcriptional regulatory elements from GRO-seq data. *Nat. Methods* **12**, 433–438 (2015).
97. H. Li, R. Durbin, Fast and accurate short read alignment with Burrows-Wheeler transform. *Bioinformatics* **25**, 1754–1760 (2009).
98. N. C. Durand, M. S. Shamim, I. Machol, S. S. Rao, M. H. Huntley, E. S. Lander, E. L. Aiden, Juicer provides a one-click system for analyzing loop-resolution Hi-C Experiments. *Cell Syst.* **3**, 95–98 (2016).
99. A. J. Saldanha, Java Treeview—Extensible visualization of microarray data. *Bioinformatics* **20**, 3246–3248 (2004).
100. T. Hulsen, J. de Vlieg, W. Alkema, BioVenn—A web application for the comparison and visualization of biological lists using area-proportional Venn diagrams. *BMC Genomics* **9**, 488 (2008).
101. E. K. Papachristou, K. Kishore, A. N. Holding, K. Harvey, T. I. Roumeliotis, C. S. R. Chilamakuri, S. Omarjee, K. M. Chia, A. Swarbrick, E. Lim, F. Markowetz, M. Eldridge, R. Siersbaek, C. S. D'Santos, J. S. Carroll, A quantitative mass spectrometry-based approach to monitor the dynamics of endogenous chromatin-associated protein complexes. *Nat. Commun.* **9**, 2311 (2018).
102. G. Dennis Jr., B. T. Sherman, D. A. Hosack, J. Yang, W. Gao, H. C. Lane, R. A. Lempicki, DAVID: Database for annotation, visualization, and integrated discovery. *Genome Biol.* **4**, P3 (2003).
103. M. Kanehisa, M. Furumichi, Y. Sato, M. Kawashima, M. Ishiguro-Watanabe, KEGG for taxonomy-based analysis of pathways and genomes. *Nucleic Acids Res.* **51**, D587–D592 (2023).
104. S. Heinz, C. Benner, N. Spann, E. Bertolino, Y. C. Lin, P. Laslo, J. X. Cheng, C. Murre, H. Singh, C. K. Glass, Simple combinations of lineage-determining transcription factors prime cis-regulatory elements required for macrophage and B cell identities. *Mol. Cell* **38**, 576–589 (2010).
105. A. Sandelin, W. Alkema, P. Engstrom, W. W. Wasserman, B. Lenhard, JASPAR: An open-access database for eukaryotic transcription factor binding profiles. *Nucleic Acids Res.* **32**, D91–D94 (2004).
106. C. E. Grant, T. L. Bailey, W. S. Noble, FIMO: Scanning for occurrences of a given motif. *Bioinformatics* **27**, 1017–1018 (2011).
107. T. L. Bailey, M. Boden, F. A. Buske, M. Frith, C. E. Grant, L. Clementi, J. Ren, W. W. Li, W. S. Noble, MEME SUITE: Tools for motif discovery and searching. *Nucleic Acids Res.* **37**, W202–W208 (2009).
108. R. Bolger, T. E. Wiese, K. Ervin, S. Nestich, W. Checovich, Rapid screening of environmental chemicals for estrogen receptor binding capacity. *Environ. Health Perspect.* **106**, 551–557 (1998).
109. S. C. Brooks, E. R. Locke, H. D. Soule, Estrogen receptor in a human cell line (MCF-7) from breast carcinoma. *J. Biol. Chem.* **248**, 6251–6253 (1973).
110. K. Ekena, J. A. Katzenellenbogen, B. S. Katzenellenbogen, Determinants of ligand specificity of estrogen receptor-alpha: Estrogen versus androgen discrimination. *J. Biol. Chem.* **273**, 693–699 (1998).
111. M. Gangloff, M. Ruff, S. Eiler, S. Duclaud, J. M. Wurtz, D. Moras, Crystal structure of a mutant hERalpha ligand-binding domain reveals key structural features for the mechanism of partial agonism. *J. Biol. Chem.* **276**, 15059–15065 (2001).

112. K. B. Horwitz, M. B. Mockus, B. A. Lessey, Variant T47D human breast cancer cells with high progesterone-receptor levels despite estrogen and antiestrogen resistance. *Cell* **28**, 633–642 (1982).
113. G. G. Kuiper, B. Carlsson, K. Grandien, E. Enmark, J. Haggblad, S. Nilsson, J. A. Gustafsson, Comparison of the ligand binding specificity and transcript tissue distribution of estrogen receptors alpha and beta. *Endocrinology* **138**, 863–870 (1997).
114. A. H. Lin, R. W. Li, E. Y. Ho, G. P. Leung, S. W. Leung, P. M. Vanhoutte, R. Y. Man, Differential ligand binding affinities of human estrogen receptor-alpha isoforms. *PLOS ONE* **8**, e63199 (2013).
115. M. S. Ozers, J. J. Hill, K. Ervin, J. R. Wood, A. M. Nardulli, C. A. Royer, J. Gorski, Equilibrium binding of estrogen receptor with DNA using fluorescence anisotropy. *J. Biol. Chem.* **272**, 30405–30411 (1997).
116. J. C. Reese, B. S. Katzenellenbogen, Differential DNA-binding abilities of estrogen receptor occupied with two classes of antiestrogens: studies using human estrogen receptor overexpressed in mammalian cells. *Nucleic Acids Res.* **19**, 6595–6602 (1991).
117. R. L. Rich, L. R. Hoth, K. F. Geoghegan, T. A. Brown, P. K. LeMotte, S. P. Simons, P. Hensley, D. G. Myszka, Kinetic analysis of estrogen receptor/ligand interactions. *Proc. Natl. Acad. Sci. U.S.A.* **99**, 8562–8567 (2002).
118. C. C. Zhang, K. A. Glenn, M. A. Kuntz, D. J. Shapiro, High level expression of full-length estrogen receptor in Escherichia coli is facilitated by the uncoupler of oxidative phosphorylation, CCCP. *J. Steroid Biochem. Mol. Biol.* **74**, 169–178 (2000).
119. M. E. Brandt, L. E. Vickery, Cooperativity and dimerization of recombinant human estrogen receptor hormone-binding domain. *J. Biol. Chem.* **272**, 4843–4849 (1997).
120. E. Jisa, A. Jungbauer, Kinetic analysis of estrogen receptor homo- and heterodimerization in vitro. *J. Steroid Biochem. Mol. Biol.* **84**, 141–148 (2003).
121. A. Tamrazi, K. E. Carlson, J. R. Daniels, K. M. Hurth, J. A. Katzenellenbogen, Estrogen receptor dimerization: ligand binding regulates dimer affinity and dimer dissociation rate. *Mol. Endocrinol.* **16**, 2706–2719 (2002).
122. C. M. Klinge, Estrogen receptor interaction with estrogen response elements. *Nucleic Acids Res.* **29**, 2905–2919 (2001).
123. F. V. Peale Jr., L. B. Ludwig, S. Zain, R. Hilf, R. A. Bambara, Properties of a high-affinity DNA binding site for estrogen receptor. *Proc. Natl. Acad. Sci. U.S.A.* **85**, 1038–1042 (1988).
124. E. W. Bergink, F. van Meel, E. W. Turpijn, J. van der Vies, Binding of progestagens to receptor proteins in MCF-7 cells. *J. Steroid Biochem.* **19**, 1563–1570 (1983).
125. R. L. Eckert, A. Mullick, E. A. Rorke, B. S. Katzenellenbogen, Estrogen receptor synthesis and turnover in MCF-7 breast cancer cells measured by a density shift technique. *Endocrinology* **114**, 629–637 (1984).
126. K. B. Horwitz, M. E. Costlow, W. L. McGuire, MCF-7; a human breast cancer cell line with estrogen, androgen, progesterone, and glucocorticoid receptors. *Steroids* **26**, 785–795 (1975).
127. P. J. Kushner, E. Hort, J. Shine, J. D. Baxter, G. L. Greene, Construction of cell lines that express high levels of the human estrogen receptor and are killed by estrogens. *Mol. Endocrinol.* **4**, 1465–1473 (1990).
128. N. Olea-Serrano, N. Devleeschouwer, G. Leclercq, J. C. Heuson, Assay for estrogen and progesterone receptors of breast cancer cell lines in monolayer culture. *Eur. J. Cancer Clin. Oncol.* **21**, 965–973 (1985).
129. J. J. Pink, S. Y. Jiang, M. Fritsch, V. C. Jordan, An estrogen-independent MCF-7 breast cancer cell line which contains a novel 80-kilodalton estrogen receptor-related protein. *Cancer Res.* **55**, 2583–2590 (1995).
130. R. M. Schoenherr, J. R. Whiteaker, L. Zhao, R. G. Ivey, M. Trute, J. Kennedy, U. J. Voytovich, P. Yan, C. Lin, A. G. Paulovich, Multiplexed quantification of estrogen receptor and HER2/Neu in tissue and cell lysates by peptide immunoaffinity enrichment mass spectrometry. *Proteomics* **12**, 1253–1260 (2012).
131. S. Shafie, S. C. Brooks, Effect of prolactin on growth and the estrogen receptor level of human breast cancer cells (MCF-7). *Cancer Res.* **37**, 792–799 (1977).
132. C. M. Taylor, B. Blanchard, D. T. Zava, A simple method to determine whole cell uptake of radiolabelled oestrogen and progesterone and their subcellular localization in breast cancer cell lines in monolayer culture. *J. Steroid Biochem.* **20**, 1083–1088 (1984).
133. T. Watanabe, J. Z. Wu, K. Morikawa, M. Fuchigami, M. Kuranami, I. Adachi, K. Yamaguchi, K. Abe, In vitro sensitivity test of breast cancer cells to hormonal agents in a radionucleotide-incorporation assay. *Jpn. J. Cancer Res.* **81**, 536–543 (1990).
134. L. E. Yaich, N. Roodi, L. R. Bailey, C. S. Verrier, C. J. Yee, D. R. Cavener, F. F. Parl, Analysis of the estrogen-receptor (ER) gene, transcript and protein in ER-positive and ER-negative breast-cancer cell-lines. *Endocr. Relat. Cancer* **2**, 293–309 (1995).
135. K. P. Yang, N. A. Samaan, Reduction of estrogen receptor concentration in MCF-7 human breast carcinoma cells following exposure to chemotherapeutic drugs. *Cancer Res.* **43**, 3534–3538 (1983).
136. P. Fernandez, R. Burghardt, R. Smith, K. Nodland, S. Safe, High passage T47D human breast cancer cells: altered endocrine and 2,3,7,8-tetrachlorodibenzo-p-dioxin responsiveness. *Eur. J. Pharmacol.* **270**, 53–65 (1994).
137. P. Fernandez, S. Safe, Growth inhibitory and antimitogenic activity of 2,3,7,8-tetrachlorodibenzo-p-dioxin (TCDD) in T47D human breast cancer cells. *Toxicol. Lett.* **61**, 185–197 (1992).
138. J. H. Clark, J. Anderson, E. J. Peck Jr., Receptor-estrogen complex in the nuclear fraction of rat uterine cells during the estrous cycle. *Science* **176**, 528–530 (1972).
139. J. H. Clark, E. J. Peck, Nuclear retention of receptor-oestrogen complex and nuclear acceptor sites. *Nature* **260**, 635–637 (1976).
140. E. Levin, A. M. Actis, S. Lopez, Characterization of rat uterine estrogen receptors in vivo. *J. Steroid Biochem. Mol. Biol.* **44**, 277–285 (1993).
141. J. Mester, E. E. Baulieu, Dynamics of oestrogen-receptor distribution between the cytosol and nuclear fractions of immature rat uterus after oestradiol administration. *Biochem. J.* **146**, 617–623 (1975).
142. E. J. Pavlik, S. Rutledge, R. L. Eckert, B. S. Katzenellenbogen, Localization of estrogen receptors in uterine cells. An appraisal of translocation. *Exp. Cell Res.* **123**, 177–189 (1979).
143. Z. Tang, B. Kang, C. Li, T. Chen, Z. Zhang, GEPIA2: An enhanced web server for large-scale expression profiling and interactive analysis. *Nucleic Acids Res.* **47**, W556–W560 (2019).

Acknowledgments: We thank the following: (i) D. Huang for helpful feedback and assistance with editing the manuscript and figures, (ii) S. Koul for additional computational support, (iii) A. Lemoff from UT Southwestern's Proteomics Core, (iv) V. Schmid from UT Southwestern's McDermott Center Next Generation Sequencing Core, (v) members of the Kraus lab for continued input and feedback on this project, and (vi) A. Dube for assistance with HiC data processing. **Funding:** This work was supported by a grant from the NIH/NIDDK (R01 DK058110) and funds from the Cecil H. and Ida Green Center for Reproductive Biology Sciences Endowment to W.L.K. **Author contributions:** Conceptualization: H.B.K. and W.L.K. Methodology: H.B.K., T.N., and Y.J.K. Investigation: H.B.K., T.N., Y.J.K., and W.L.K. Formal analyses: H.B.K., T.N., and W.L.K. Software: H.B.K. and T.N. Validation: H.B.K., T.N., C.V.C., and W.L.K. Visualization: H.B.K., T.N., and W.L.K. Writing—original draft: H.B.K., C.V.C., and W.L.K. Writing—review and editing: H.B.K., C.V.C., and W.L.K. Resources: W.L.K. Funding acquisition: W.L.K. Supervision: C.V.C. and W.L.K. Project administration: C.V.C. and W.L.K. **Competing interests:** The authors declare that they have no competing interests. **Data, code, and materials availability:** All data and code needed to evaluate and reproduce the conclusions in the paper are present in the paper and the Supplementary Materials or are publicly available. This paper contains new data generated from genomic assays (RNA-seq, ChIP-seq, ATAC-seq, PRO-seq, and HiC) and proteomic assays (RIME) (refer to the corresponding sections of Materials and Methods). The raw data from these genomic assays can be accessed from the Gene Expression Omnibus (GEO) database of National Center for Biotechnology Information (NCBI) (www.ncbi.nlm.nih.gov/geo/) using the following accession numbers: GSE298771 (RNA-seq), GSE298767 (ChIP-seq), GSE298769 (ATAC-seq), GSE298770 (PRO-seq), and GSE318617 (HiC) under the super series accession number GSE298773. The raw RIME proteomics data can be accessed from the Mass Spectrometry Interactive Virtual Environment (MassIVE) database (https://massive.ucsd.edu/ProteoSAFe/static/massive.jsp?redirect=auth) using accession number MSV000098072. Author-created physical materials can be obtained upon request to the corresponding author at lee.kraus@utsouthwestern.edu. Publicly available ERα ChIP-seq data from samples from patients who have breast cancer treated with the aromatase inhibitor can be accessed from NCBI GEO using accession number GSE40867 (*62*).

Submitted 12 September 2025
Accepted 23 April 2026
Published 3 June 2026
10.1126/sciadv.aec2424